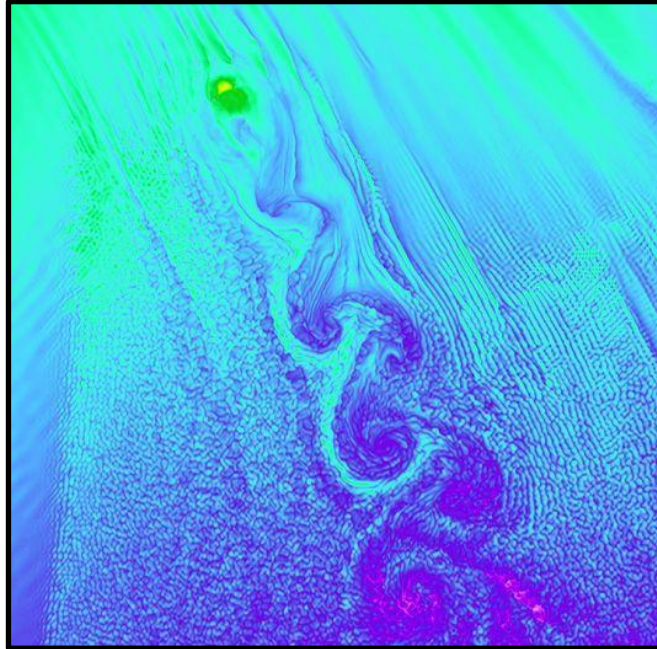


Kármán Vortex Street Energy Harvester for Picoscale Applications



22 March 2018

Team Members:

James Doty
Christopher Mayforth
Nicholas Pratt

Advisor:

Professor Brian Sivilonis

A Major Qualifying Project
submitted to the Faculty of
WORCESTER POLYTECHNIC INSTITUTE
in partial fulfilment of the requirements for the
degree of *Bachelor of Science*

This report represents work of WPI undergraduate students submitted to the faculty as evidence of a degree requirement. WPI routinely publishes these reports on its web site without editorial or peer review. For more information about the projects program at WPI, see <http://www.wpi.edu/Academics/Projects>.

Cover Picture Credit: [1]

Abstract

The Kármán Vortex Street, a phenomenon produced by fluid flow over a bluff body, has the potential to serve as a low-impact, economically viable alternative power source for remote water-based electrical applications. This project focused on creating a self-contained device utilizing thin-film piezoelectric transducers to generate hydropower on a pico-scale level. A system capable of generating specific-frequency vortex streets at certain water velocities was developed with SOLIDWORKS modelling and Flow Simulation software. The final prototype nozzle's velocity profile was verified through testing to produce a velocity increase from the free stream velocity. Piezoelectric testing resulted in a wide range of measured dominant frequencies, with corresponding average power outputs of up to 100 nanowatts. The output frequencies were inconsistent with predicted values, likely due to an unreliable testing environment and the complexity of the underlying theory. A more stable testing environment, better verification of the nozzle velocity profile, and fine-tuning the piezoelectric circuit would allow for a higher, more consistent power output.

Table of Contents

Abstract.....	1
1. Introduction.....	7
2. Literature Review.....	8
2.1 Types of Run-of-River Hydropower.....	8
2.2 The Kármán Vortex Street.....	10
2.2.1 Vortex Shedding.....	11
2.2.2 Vibrations.....	12
2.2.3 Kármán Vortex street as an energy source.....	13
2.3 Past Works.....	13
2.3.1 Eel Harvester Method.....	13
2.3.2 Oscillating Bluff Method.....	15
2.3.3 Previous MQP's.....	15
2.4 Piezoelectric Energy Harvesting.....	16
2.4.1 Piezoelectric Materials.....	16
2.4.2 How Piezoelectrics Operate.....	17
2.4.3 Power Output from Piezoelectrics.....	17
3. Kármán Vortex Street Energy Harvester Design.....	20
3.1 General Simulation Methods.....	20
3.1.1 Standard Boundary Conditions.....	20
3.1.2 Computational Domain.....	21
3.1.3 Mesh Sizes.....	21
3.2 Oscillating Bluff Body Design.....	21
3.2.1 Preliminary Design.....	21
3.2.2 Preliminary Calculations.....	23
3.2.3 Preliminary Sketches/Drawings.....	25
3.2.4 Determining the Aspect Ratio.....	25
3.2.5 Force Analysis.....	27
3.3 Eel Harvester Design.....	29
3.3.1 Preliminary Eel Harvester Design.....	29
3.3.2 Preliminary Calculations.....	30
3.3.3 Preliminary Sketches/Drawings.....	31
3.3.4 Flow Simulations to Revise Nozzle Design.....	33
3.3.5 Determining the Redesigned Nozzle Aspect Ratio.....	39
3.3.6 Determining the Minimum Bluff Body Diameter.....	41
3.3.7 Final Eel Nozzle Design.....	43
3.4 Bluff Body Mechanism Design.....	45
4. Nozzle Construction Process.....	51
5. Testing and Analysis.....	53
5.1 Testing Methodology.....	53
5.1.1 Building the Testing Rig.....	54

5.2 Nozzle Velocity Profile.....	54
5.2.1 Pressure Transducers and Calibration	55
5.2.2 Pressure Transducer Calibration Results	55
5.2.3 Velocity Profile Testing Initial Results	57
5.2.4 Recalibration and Final Velocity Profile Results	59
5.3 Piezoelectric Testing	60
5.3.1 Piezoelectric Testing Power Output Results.....	60
5.3.2 Piezoelectric Testing Frequency Results	61
5.4 Results Discussion.....	63
5.4.1 Power Output.....	63
5.4.2 Frequency	63
6. Conclusions.....	65
6.1 Testing.....	65
6.2 Theory	65
6.3 Further Considerations.....	66
6.4 Potential Applications.....	66
References:.....	67
APPENDIX A: MATLAB Script for Mechanism Design.....	69
APPENDIX B: Fast Fourier Transform Chart for Piezoelectric Output Data.....	70

List of Figures

Figure 1: Suggested Turbines for Different Flow Rates and Head Levels [4]	9
Figure 2: Alexander Gorlov's chart of turbine-based hydrokinetic technologies [5]	10
Figure 3: The von Kármán Vortex Street. [7].....	11
Figure 4: Geometry of an Oscillating Membrane Behind a Flat Plate [12].....	13
Figure 5: The Piezoelectric Harvester Setup Used by Koyvanich et. all [15]	14
Figure 6: How VIVACE Works [16].....	15
Figure 7: Three Simple Diagrams of how a Piezoelectric Transducer Operates [19]	17
Figure 8: Example Resonant Frequency vs. Power Output Graph for select Piezoelectrics [21]	18
Figure 9: A circuit model of a piezoelectric. [20].....	18
Figure 10: An example circuit diagram of a rectifying circuit [24].....	19
Figure 11: Preliminary Design for the Oscillating Bluff Body.....	22
Figure 12: Preliminary Design of the Multi-Oscillating Bluff System.....	23
Figure 13: Preliminary Design of the Bluff Body within the Duct.....	25
Figure 14: Vortex Street at 0.493 seconds for an Aspect Ratio of 5	26
Figure 15: Vortex Street at 0.509 Seconds for an Aspect Ratio of 5.....	27
Figure 16: 16a (left)/16b (right), Preliminary Designs for the "Eel" Harvester	29
Figure 17: Front View of the Free End Configuration	31
Figure 18: Front View of the Fixed End Configuration	32
Figure 19: Cross-Section Top View	33
Figure 20: The Redesigned Nozzle.....	34
Figure 21: A graphical representation of the first parametric study results.....	36
Figure 22: A graphical representation of the second parametric study results.	38
Figure 23: Evidence of the Nozzle Generating Vortices.	39
Figure 24: SOLIDWORKS Flow Simulation Setup for Determining Aspect Ratio.	40
Figure 25: Vortex Street Generation Shown for Fixed End Configuration, Aspect Ratio 4.	41
Figure 26: Final Nozzle Design	43
Figure 27: Bottom Piece of the Nozzle.....	44
Figure 28: Top Piece of the Nozzle	45
Figure 29: Mechanism to Change the Bluff Body Length based on Flow Speed.....	46
Figure 30: Mechanism Base.....	48
Figure 31: Mechanism Rod.....	48
Figure 32: Mechanism Buffer Post.....	49
Figure 33: Top View of Mechanism Disk	49
Figure 34: Bottom View of Mechanism Disc	50
Figure 35: The Fully Manufactured Nozzle.....	52
Figure 36: The WPI Crew Team Rowing Tank.....	53
Figure 37: The Testing Rig in the Rowing Tank	54
Figure 38: The Pressure Transducer Calibration Pipe Setup	55

Figure 39: The Initial Unmarked Pressure Transducer Calibration Data	56
Figure 40: The Initial Marked Pressure Transducer Calibration Data.....	56
Figure 41: The Control Panel for the Rowing Tank	57
Figure 42: The Pitot Tube within the Nozzle.....	58
Figure 43: The First Nozzle Velocity Profile	58
Figure 44: The Updated Unmarked Transducer Calibrations.....	59
Figure 45: The Updated Marked Transducer Calibrations	59
Figure 46: The Nozzle Velocity Profile after Recalibration.....	60
Figure 47: An example output chart of the frequency data.	62

List of Tables

Table 1: The Forces on the Cylinder.....	28
Table 2: The results of the first 2D parametric study	35
Table 3: The results of the second 2D parametric study.....	37
Table 4: Results of the Minimum Diameter Simulations	42
Table 5: The Manufactured Bluff Body Sizes.	51
Table 6: Piezoelectric Power Output Data.....	61
Table 7: Piezoelectric Frequency Data	62
Table 8: The Target vs. Actual Frequencies	63
Table 9: The Strouhal Numbers and Estimated Velocity Increases of the Nozzle.....	64

1. Introduction

Agencies such as the United States Geological Survey rely on large systems of aquatic sensors to monitor bodies of water. These networks provide real-time data on stream flows, water levels and water quality. This information is critical to agencies in the event of a flood or drought and can help illustrate the effect of climate change on streams over time [2]. Expanding these networks will require a large number of self-reliant sensors to be placed in remote areas that would require their own power source. Currently there are sensors available that operate with batteries or solar panels, but these power sources still limit sensor location. Battery powered sensors need to be placed in an easily accessible area, and solar panel powered sensors require consistent access to sunlight. Ideally a sensor would draw energy from the stream it is located in, with little maintenance required beyond the initial setup.

A viable method for powering remote sensor systems would be to directly harvest energy from the streams they are monitoring. Hydropower is a reliable source of energy and can often boast a capacity factor far beyond that of solar or wind power. This is largely due to the consistency of stream flow. Aside from seasonal fluctuations, the flow is usually constant. This is useful for a sensor that needs to reliably log and transmit data, as opposed to wind or solar energy sources that depend on the intermittent availability of wind or sunlight.

Hydropower has predominantly manifested in head-based hydroelectric turbines. Head denotes the difference in surface elevation from upstream to downstream, commonly seen in dammed sections of rivers. Use of head-based hydropower requires the nearby presence of a dam or natural drop in surface water elevation, such as a waterfall. Use of this for a remote sensor would limit potential deployment locations. Other hydrokinetic systems take the form of axial turbines, utilizing either horizontal or vertical axis designs. However, the use of these systems for a micro-scale hydropower application would be difficult as conventional turbine efficiency greatly reduces at smaller sizes due to reduction in blade surface area and increased friction in the bearings [3]. This has led to the development of alternative, non-turbine hydrokinetic energy harvesting innovations. One of these emerging innovations is to harvest the energy of vortex induced vibrations.

The goal of this project is to prototype a device that utilizes piezoelectric transducers to harvest electrical energy through vortex street generation in stream flow. This device will be designed for use in remote low-power applications, such as river-based water quality sensors. We found that the power requirements of these application range from around 400mW for all-in-one sensor systems down to 10nW for some experimental pressure and temperature sensors [4][5]. Modern remote sensor technology relies on photovoltaic cells and batteries; however, they are not always a feasible source of electricity. This project aimed to provide a reliable alternative power source to meet this need.

2. Literature Review

In this section, background material that is pertinent to understanding how vortex street theory can be applied to an energy harvesting scenario will be described. First, different types of hydropower technologies are discussed, followed by vortex street theory and Kármán vortex street generation. Next, previous attempts at energy harvesting from vortex streets are then analyzed, and finally piezoelectric technology is analyzed.

2.1 Types of Run-of-River Hydropower

Use of run-of-river hydropower enables the deployment of remote sensors wherever there is a nearby stream. Run-of-river denotes that the hydropower technology does not disrupt the flow or level of the stream. A pumped hydroelectric storage or dammed reservoir would therefore not fall into this category. Technologies that fall into these categories can be primarily split into two groups: head-based and hydrokinetic.

Head-based hydropower technologies comprise most conventional hydroelectric projects. They operate by capturing the gravitational potential energy of water at a dam or natural drop in stream elevation. This is largely a factor of the difference between the upstream and downstream surface water elevations, or head.

Head and flow rate determines the type of turbine used. Very large head operations generally employ Pelton or Francis turbines, while lower head operations often use Kaplan turbines (Figure 1). At optimal conditions, these turbines can operate at efficiencies exceeding 90%. As these turbines operate at very high rotational speeds, generally greater than 100 RPM, they require inlet screening to minimize damage to both aquatic life and the turbine blades [6]. Archimedes Screw turbines utilize a slowly-rotating angled screw to capture the energy of stream flow as it lowers in elevation. This technology has been proven to safely pass fish downstream and requires minimal screening. A main drawback is a lower efficiency of roughly 70% due to increased mechanical losses as the lower RPMs must be amplified via a gearbox before application to a generator [6]. Head-based hydropower offers a useful solution to small or large-scale renewable energy production; however, it is limited to locations with a head to capture energy from, and the technologies used do not efficiently scale down to the watt or milliwatt level.

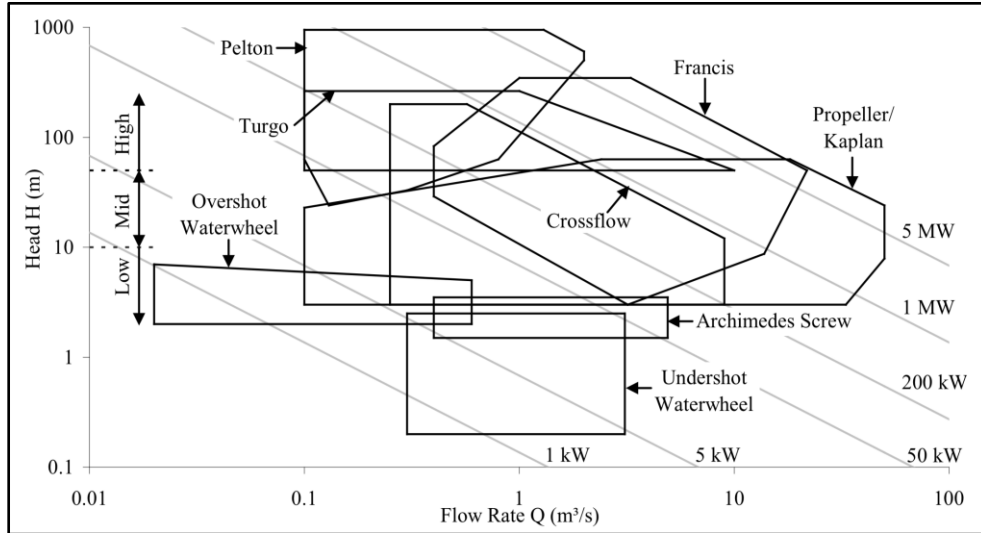


Figure 1: Suggested Turbines for Different Flow Rates and Head Levels [4]

Hydrokinetic power technologies offer the capability of being located wherever there is a flow, with or without a head, as they operate by capturing the kinetic energy from a flow. Many innovations in hydrokinetic energy parallel those of wind power, as both utilize the same principle of taking energy from a flowing fluid. As such, horizontal and vertical axis turbines have been developed for hydropower applications that closely resemble their dryland counterparts. Tyson, Garman, and marine turbines comprise the leading horizontal axis turbines, while Darrieus, Gorlov, Savonius, and Curtate turbines make up the forefront of vertical axis turbine innovation. As can be seen in Figure 2, vertical axis turbines have higher efficiencies, with some nearing the 50% mark [7]. This efficiency can be compared to the theoretical maximum efficiency of 59%. This maximum value has been derived from the basis that, although the goal is to capture all of the flow energy, a zero flow out of a turbine would prevent flow through the turbine due to the principle of mass conservation. These turbines suffer from the same scaling down issue as head-based hydropower. As Zhu described, turbines scale down poorly due to the increase in frictional losses in the bearings and decreased surface area of the turbine blades [3]. This has led to the pursuit of specific micro-scale hydropower technologies, including those harvesting Kármán vortex street energy.

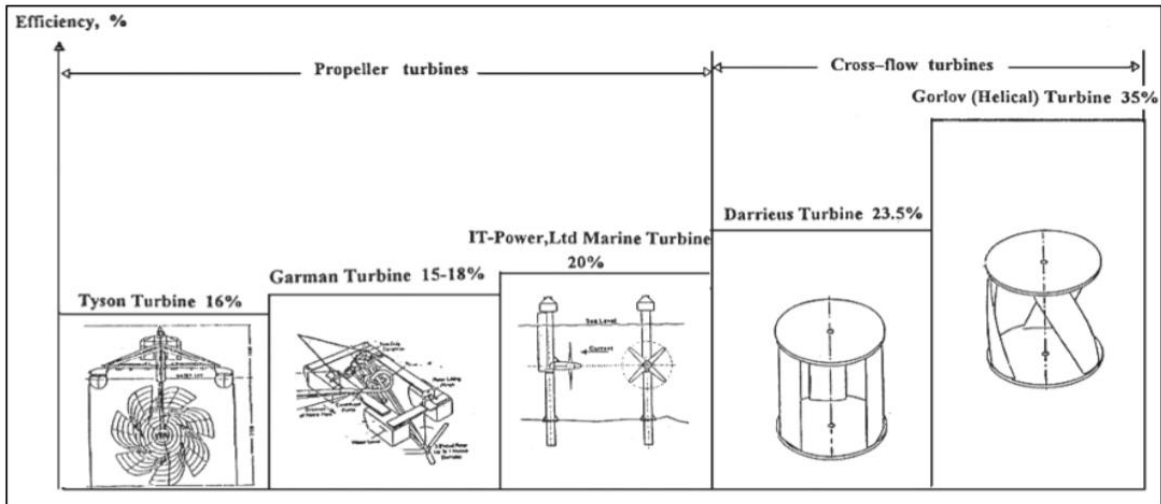


Figure 2: Alexander Gorlov's chart of turbine-based hydrokinetic technologies [5]

2.2 The Kármán Vortex Street

When a fluid flows over a blunt object, also referred to as a bluff body, such as the white circle in Figure 3, the flow causes a Kármán vortex street. The vortex street refers to the periodic formation of vortices on alternating sides of the body in the direction of the flow. This phenomenon occurs in slightly different patterns in Reynolds numbers ranging between 150 and 3×10^5 . It occurs as the result of alternating pressures behind the bluff body so if something is placed directly behind the body, vortex generation will be stunted. Energy from this vortex generation can currently be harvested in a few ways, such as using the lift force on the bluff body itself, or by using the pressure difference to bend a piezoelectric sheet. The benefit of utilizing vortex streets as an energy source is how it only depends on the geometry of the bluff body and the fluid velocity; as long as the flow continues the vortices will be generated. This makes vortex street-based energy harvesting an ideal way to power systems in remote areas where there is a readily available water flow [10].

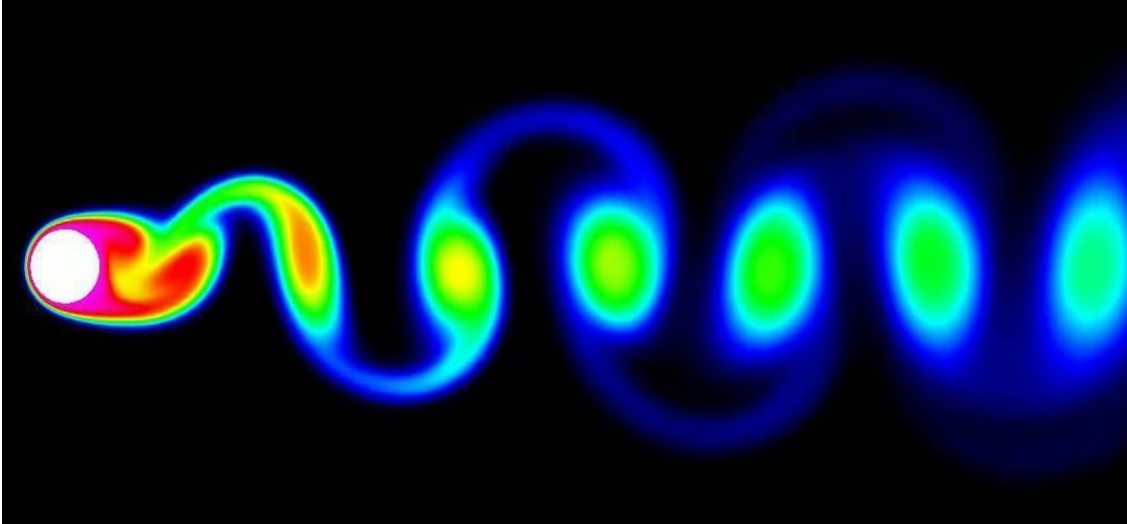


Figure 3: The von Kármán Vortex Street. [7]

2.2.1 Vortex Shedding

The Strouhal number St predicts the frequency of the vortices shedding, and is given as:

$$St = \frac{f * D}{U} \quad (1)$$

Where f is the vortices generation frequency, D is the characteristic length of the bluff body, and U is the mean speed of the fluid. The Strouhal number is generally approximated to be ~ 0.2 but is a function of the Reynolds number Re given by the Roshko number Ro : [8]

$$Ro = St * Re \quad (2)$$

Where the Roshko number is:

$$Ro = 0.212 * Re - 4.5 \text{ for } 50 \leq Re < 200 \quad (3)$$

$$Ro = 0.212 * Re - 2.7 \text{ for } 200 \leq Re < 2000 \quad (4)$$

The second equation can be used to approximate the Strouhal number for ranges above a Reynolds number of 2000. However, it is less accurate at higher Reynolds numbers, and gives approximately 4% error by 10,000 [10]. The proximity of the bluff body to a wall affects the vortex generation. When taking this into account, the adjusted Strouhal equation is characterized by:

$$St = g_h * St_{\infty(Re)} \quad (5)$$

Where g_h is the adjustment parameter for the Strouhal number, and St_∞ is the Strouhal number without the presence of a wall. Rosemary Matty experimentally determined the parameter g_h for a flat plate to be:

$$g_h = 1 + 0.518 * e^{(-4.6 * \frac{h}{L})} * \sin \left[\frac{18 * \pi}{180} * (20 * \frac{h}{L} - 1) \right] \quad (6)$$

Where h is the gap between the bluff body and the wall, and L is the height of the bluff body. The correlation is accurate to within 5% for most Reynold numbers, but reached 10% at low Reynolds numbers. However, the error analysis for Matty's experiment showed that this error at low Reynolds number was expected due to the testing equipment [11].

Previous research indicates that for low aspect-ratio flat plates, the vortex street will irregularly rotate around the edge of the bluff body; however, the frequency of the rotation slows as both the aspect ratio and Reynolds number increase [12]. Kármán vortex streets eventually break down due to instabilities; this distance for a cylindrical bluff body was found by a researcher at the Florida Atlantic University [13]:

$$x_{bd} = \frac{4 * \gamma^2 * Re}{15 * \pi * St} \quad (7)$$

Where Re is the Reynold Number, St is the Strouhal Number, and γ is a non-dimensional number, found from the mean value of the non-dimensional flow deficit where u is the velocity of the fluid:

$$\gamma = 1 - \frac{\sqrt{2}}{2} (1 - u) \quad (8)$$

2.2.2 Vibrations

The vortex street can cause the bluff body to vibrate. This is caused by the variation in lift and drag that results from the alternating vortices generation. The lift force oscillates at the same frequency as the vortex generation, while the drag force oscillates at double the frequency. For a cylinder these are given by:

$$L_{(t)} = L_0 * \cos (\omega_s * t + \varphi) \quad (9)$$

$$D_{(t)} = D_0 * \cos (2 * \omega_s * t + \varphi) \quad (10)$$

Where omega ω is the vortex shedding frequency in radians, t is time, and phi φ is the phase angle. This causes an unrestrained bluff body to move in a figure-eight path [8].

2.2.3 Kármán Vortex street as an energy source

The hydropower industry largely consists of turbine-based operations; however, an increasing number of applications suitable for ‘micro’ scale hydropower systems has led to the exploration of using Kármán vortex streets as an energy source. As seen in the previous section, vortex street theory has developed to the point where it can be modeled and predicted. This then leads to a theoretical value of the energy that can be extracted from these shed vortices.

Previous works have identified several methods for harvesting vortex street energy. These can be categorized as the eel harvester and oscillating bluff methods. These methods transfer vortex energy into mechanical energy through the use of an object in the flow path. The transfer of mechanical energy into electrical energy has generally been accomplished via a variety of methods, such as piezoelectric materials, electromagnets, and crankshafts.

2.3 Past Works

Previous work relating to energy harvesting from vortex streets must be analyzed. There are a few different ongoing developments that have produced various potential solutions, including eel-type designs and oscillating bluff-type designs. Additionally, there have been a few previous WPI MQP’s that have worked with both piezoelectric vibration energy harvesting and vortex street energy harvesting.

2.3.1 Eel Harvester Method

Allen & Smits (2000) examined the use of a static bluff body with a dynamic membrane or “eel” in its wake, as a means of capturing hydrokinetic energy (Figure 4). Much of their work was directed at deriving equations to model the behavior of a flexible membrane as it experiences the force of the vortex shedding from an upstream bluff body [14].

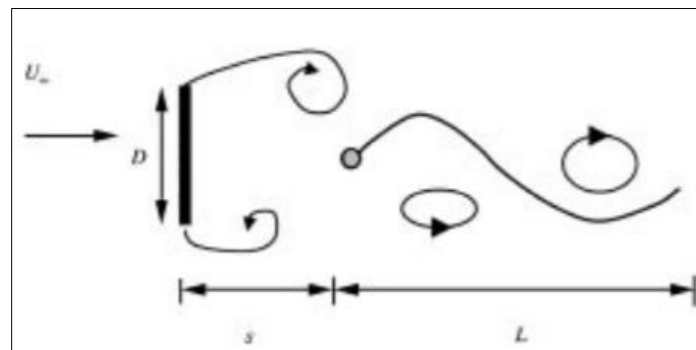


Figure 4: Geometry of an Oscillating Membrane Behind a Flat Plate [12]

Allen & Smits determined that there is a “lock-in” behavior, characterized as occurring “when the membranes oscillate at the same frequency as the undisturbed wake behind a bluff body.” [14]

They empirically found that lock-in will take place when:

$$\frac{0.2\xi_n U_\infty^2 \rho W}{\rho_{eel}(-\omega_{eel}^2 + \omega_n^2)D} > 1 \quad (11)$$

Where $\xi_n(t)$ is the modal function, U is the free stream velocity, ρ is the fluid density, W is the width of the film, ρ_{eel} is the film density, ω_{eel} is the vibration frequency of the eel, ω_n is the natural frequency of the eel film, and D is the characteristic length of the bluff body.

During lock-in the membrane will also oscillate with an amplitude similar to the width of the wake. Therefore, the lock-in condition should be met in order to optimize a piezo film-based energy harvesting device. The group found that there is a significantly higher sensitivity to bluff body size compared to membrane length; it will be important to find the optimal characteristic length of the bluff body [14].

Koyvanich, Smithmaitrie, and Muensit examined the energy extraction capabilities of a piezoelectric harvester [15]. Their testing apparatus and setup can be seen in Figure 5. Koyvanich et.al. conducted their experiment at a 6.8m/s velocity and a 0.4 Hz oscillating frequency. Using a flexible PVDF thin-film piezo with a 1M Ω load, they generated 6.6 mV and produced a maximum power output of 0.18 μ W. From a 44 μ W potential power, this correlated to a 0.41% efficiency for their system. They state that “this is the performance of a single piezo-generator. An increase in η can be developed by producing multiple arrays of the harvester, so that the P_{elec} is increased at a constant P_{flow} .” [15]

Where:

$$P_{flow} = \frac{1}{2} \rho A U^3 \quad (12)$$

$$P_{elec} = \frac{2V_{RMS}^2}{R} \quad (13)$$

And

$$\eta = P_{elec}/P_{flow} = \frac{V_{rms}^2}{R\rho AU^3} \quad (14)$$

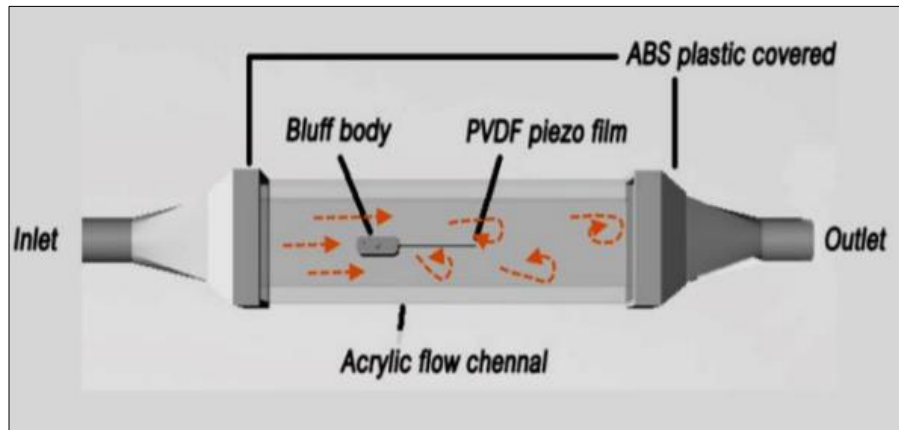


Figure 5: The Piezoelectric Harvester Setup Used by Koyvanich et. al. [15]

2.3.2 Oscillating Bluff Method

The oscillating bluff method is best displayed in the works of Bernitsas and co. at the University of Michigan in their development of the *Vortex Induced Vibrations for Aquatic Clean Energy (VIVACE)* converter, shown in Figure 6. The work done by the university stands out from other examples of Vortex Induced Vibration (VIV) energy harvesters as their device is much larger. Most VIV devices are in the early stages of development, and typically stand in the micro-scale. However, Bernitsas and his team have been developing the *VIVACE* concept for the past decade and have tested a ‘small-scale’ device capable of producing power in the watts to kilowatts range. The *VIVACE* device utilizes large boxes containing horizontal cylinders which oscillate up and down due to the lift force acting on them from vortex shedding. The oscillations of the cylinder are transferred to electrical power via an electromagnetic system in place on the sides of the box. This power is then inverted from DC to AC and so it can then be transmitted to the power grid. The *VIVACE* system boasts an energy density between 2 and 10 times that of most other marine energy converters. This example specifically illustrates the potential that VIV based energy harvesters have to shape the development of the renewable energy industry [16].

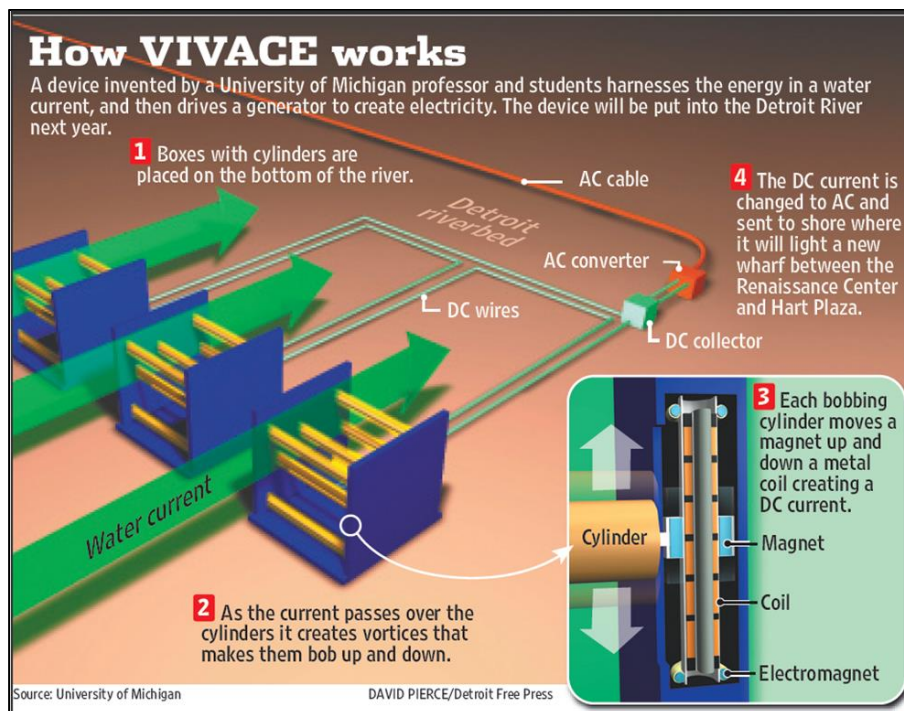


Figure 6: How VIVACE Works [16]

2.3.3 Previous MQP's

WPI students Diltz, Gagnon, O'Connor, and Wedell in their 2016-2017 MQP utilized piezoelectric transducers to extract energy from the vortex induced vibration (VIV) oscillations of a cylindrical body in flowing water. The group was able to create a prototype capable of producing a 12mm average amplitude at a 3.2 Hz frequency. They were able to extract around 0.1 μ W via their piezoelectric transducers; however limited testing conditions kept them from

producing an accurate output measurement. The group used a frame that suspended the device from the surface of the water. The cylindrical body was fixed to springs on this frame with the cylinder's axis positioned normal to the flow direction and parallel to the water surface. Their system had an estimated mechanical efficiency of 28.8%, but an electrical efficiency of 0.000053%. This identifies that although there are potential mechanical systems to harvest Kármán vortex street energy, there must be ample consideration put into optimizing mechanical to electrical conversion prior to successful application [17].

WPI students Distler, Johnson, Kielbasa, and Phinney in their 2010-2011 MQP compared various shapes as the subject of the forces exerted through vortex shedding [18]. They determined that "T" shapes generate 40% greater amplitudes and 50% greater forces than cylinder shapes, but cylinders had a frequency 85% higher than "T" shapes. The work done by this group provides a useful reference for determining a bluff body shape for this project's application. The group also showed that from their testing, the cylindrical design produced a higher power output due to the greater frequency. As a result, a cylindrical bluff body appears best suited for this application.

2.4 Piezoelectric Energy Harvesting

Piezoelectricity is the term for electric charge generated from oscillatory mechanical strain on certain crystals, ceramics, and biological materials. The piezoelectric effect is used in many different devices, such as echolocation systems, electric ignition lighters, acoustic guitar pickups, loudspeakers, clocks, and inkjet printers [19]. One emerging application of the piezoelectric effect is the ability for it to be used for energy harvesting in situations involving oscillatory motion. Piezo transducers availability in many shapes, sizes, materials, and resonant frequencies, enable their effective application to many energy-harvesting situations.

2.4.1 Piezoelectric Materials

Most commercial piezoelectric materials are quartz crystals, or ceramics such as barium titanate, lead titanate, and PZT (lead zirconate titanate). Commercially, quartz is the most commonly utilized crystal piezo, while PZT is the most common ceramic because of its high material strength, durability, and comparatively low cost [20]. Additionally, flexible thin-film piezoelectrics such as polyvinylidene fluoride (PVDF) are becoming increasingly popular for applications that involve larger amplitudes. These generally work less efficiently and at a much lower frequency than other materials. When choosing a suitable piezo for a specific application, the piezo capacitance, resonant frequency, maximum voltage, and maximum deflection are important to consider [17].

Different piezoelectric materials have different properties depending on how they are oriented and operated. A piezo element's modulus of elasticity and stiffness do not generally vary with direction, so they can be treated as constants. The piezoelectric charge constant serves as an indicator of the electric potential developed. The dielectric constant, which is the ratio of the material's permittivity to the permittivity of free space, varies with the direction the element is operated in, however this variance is relatively insignificant. The electromechanical coupling

coefficient represents the material's ability to convert mechanical energy to electrical energy. The coupling coefficient is generally greater for a rectangular plate lengthwise than for a disk element [17]. Electromechanical coupling coefficients are generally higher for crystal and ceramic materials than films. For example, the electromechanical coupling of PFVD is between 0.12 and 0.14, while PZT ranges from 0.35 and 0.65.

2.4.2 How Piezoelectrics Operate

To generate electricity from a piezoelectric, the material must be cyclically strained. This deforms the internal structure of the material, causing the separation of the positive and negative gravity centers of the molecules, which generates dipoles that polarize the material (Figure 7). This polarization generates an electric field which can be used to transduce electrical energy from mechanical motion.

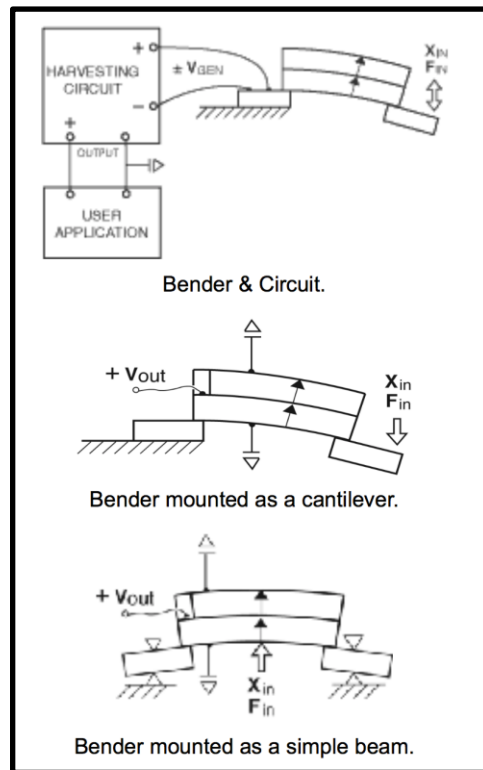


Figure 7: Three Simple Diagrams of how a Piezoelectric Transducer Operates [19]

2.4.3 Power Output from Piezoelectrics

The amount of electrical charge generated is proportional to the amount of strain. Piezoelectricity depends on a combination of the linear electrical behavior of a material (D) and Hooke's law for linear elastic materials (S).

$$D = \epsilon E \quad (15)$$

$$S = sT \quad (16)$$

Where D is the electric displacement [C/m^2], ϵ is the dielectric constant [F/m], and E is the electric field strength [N/C]. In Equation 16, S is strain [m/m], s is the compliance [m^2/N],

and T is stress $[\text{N}/\text{m}^2]$. These two equations combine with the matrix of electric permittivity to model the piezoelectric effect.

To get the most electrical power out of a piezoelectric element, the strains must be cyclical and as close to the manufacturer-specified frequency as possible. Most piezoelectric transducer manufacturers have readily available power versus frequency graphs (Figure 8) that show the power output based on acceleration amplitude, mass damping, and the operating input frequency [20].

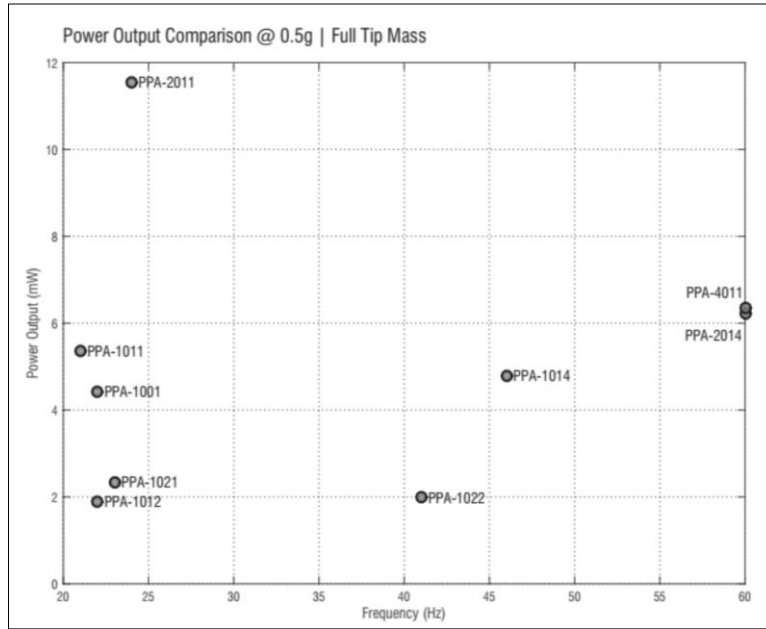


Figure 8: Example Resonant Frequency vs. Power Output Graph for select Piezoelectrics [21]

The circuit model in Figure 9 illustrates the internal circuit of a piezoelectric element. Equation 20 models the output voltage of the piezoelectric. C_o is the electrical capacitance arising from the dielectric material placed between the two electrodes of the piezo element. The current i_p induced by the piezoelectric effect in a material is equivalent to a circuit formed by resistance R_m , an inductance L_m , and a capacitance C_m . All of these values are available in the data sheets of a given piezoelectric element [22].

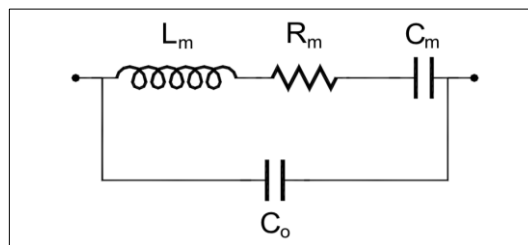


Figure 9: A circuit model of a piezoelectric. [20]

$$V = R_m i_p + L_m \frac{di_p}{dt} + \frac{1}{C_m} \int i_p dt \quad (17)$$

Piezoelectric transducers output an AC signal, so many vibration-based energy harvesting systems use the piezo element as an AC power source. In order to utilize a DC current, such as one that would supply power to a sensor, the output voltage must be rectified and regulated to a constant voltage [24]. An example of this is shown in Figure 10.

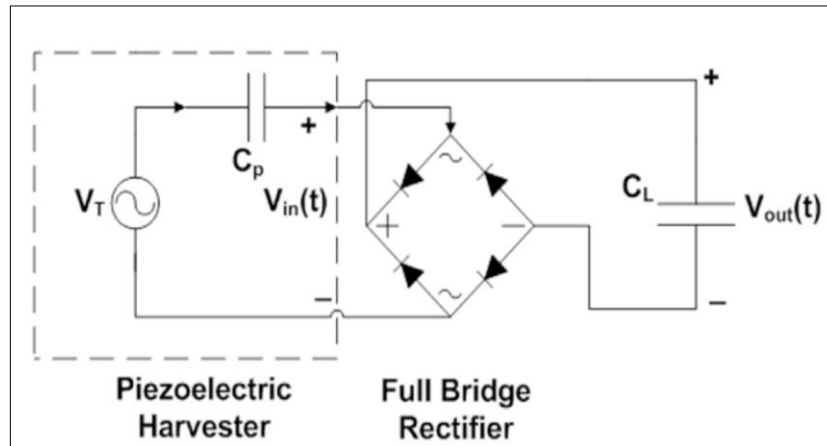


Figure 10: An example circuit diagram of a rectifying circuit [24]

3. Kármán Vortex Street Energy Harvester Design

This project aimed to optimize the eel and oscillating bluff body methods by creating designs capable of adapting to variable flow speeds, from 0.0 to 3.0 m/s. We considered two methods of using piezoelectrics to convert the vortex streets to electrical energy. One method uses an oscillating bluff body to vibrate connected piezoelectric materials, while another uses a piezoelectric film suspended behind the bluff body, which we refer to as the Eel Harvester Design. The goal of each design was to control the frequency of the vortex streets, which the Oscillating Bluff Body Design would do by controlling the incoming flow velocity, and the Eel Harvester design would do by varying the size of the bluff body.

First, the basic design of the systems was completed by relating vortex street equations to determine relative component sizing. To determine the exact dimensions of the nozzle and the bluff bodies, 2D and 3D flow simulations were performed using SOLIDWORKS Flow Simulation software. Through iterative analysis of these simulations, the nozzle and bluff body dimensions were optimized to allow the maximum frequency at the low velocity flows with regard to vortex generation potential, sizing restrictions, and manufacturability concerns. During the nozzle simulations discussed in Section 3.2.1 we realized that we were unable to consistently predict how variations in nozzle area would affect flow speed, which was the premise of the Oscillating Bluff Body design. While the design considerations for this design are discussed below, we ultimately pursued the Eel Harvester design.

3.1 General Simulation Methods

For our simulations we used SOLIDWORKS Flow Simulation software. The ease of use and the ability to easily vary model dimensions in parametric simulations made it ideal for our use case. Like other fluid simulation software, it allows you run internal or external, 2D or 3D simulations, with a variety of boundary conditions. These conditions are all specified when the specific simulations are discussed below in Sections 3.2 and 3.3, but here is a brief explanation of the general process used to run the simulations.

3.1.1 Standard Boundary Conditions

Since in all of our simulations we are attempting to recreate the flow in a river, the boundary conditions are fairly consistent throughout each internal and external flow simulation. For internal flows, which were used to model conditions in the nozzle to determine the throat dimensions and bluff body sizes, the boundary conditions were always that the incoming velocity was the expected velocity increase from the nozzle times the free stream velocity, and the exit pressure was always the “environmental pressure” (101 kPa). For the external flow simulations which were used to determine the nozzle shape, the flow in the x-direction, which corresponded to the incoming flow, was set to be the free stream velocity, while the ambient pressure was set to be 101 kPa.

3.1.2 Computational Domain

When the simulation is created, either a 2D or a 3D computational domain is assumed by the SOLIDWORKS Flow Simulation software. Unless otherwise specified by the specific simulation, this is the computational domain that was used. After each simulation we checked the pressure and velocity plots to make sure that the boundary conditions were not violated, which would require increasing the size of the computational domain until they were not.

3.1.3 Mesh Sizes

SOLIDWORKS Flow Simulation software has a unique way of controlling mesh size. It allows you to change the mesh size using a setting called the “general mesh,” that has a sliding bar scale from 1 to 7, with a lower number corresponding to a coarser mesh. In each case we added a “local mesh” around the bluff body during the simulations for the nozzle throat dimensions, or around the nozzle for the simulations that were used to optimize the nozzle size. Like the general mesh, the local mesh was controlled with a sliding scale from 1 to 7, but the local mesh increases the density of the meshes in that area. For example, in a 2D simulation a local mesh setting of 2 would add 4 meshes into an area that previously had one, a setting of 3 would have 9, etc.

SOLIDWORKS Flow Simulation also attempts to guess the desired mesh size. In order to make sure that the meshes were high enough and that the results had converged, the initial simulation for each set was run again at higher settings, and the results compared. If the results were significantly different, then the mesh settings were increased, and the simulations run again. Each discussion of a specific set of simulations reports the general mesh and local mesh settings that were used.

To determine optimal mesh sizes, each mesh was individually adjusted in order to choose the highest mesh size values that would still run in a reasonable time frame. Given the time scale and limited computational resources available to this project, a “reasonable time frame” was generally considered to be around two days or less of estimated computation time.

3.2 Oscillating Bluff Body Design

The oscillating bluff method utilizes the induced lift force applied to a cylindrical bluff body placed in the flow. In this method, the vortices themselves do not apply a force to the body, but rather the shedding of vortices by a bluff body causes periodic lift and drag forces on that body. A previous MQP group investigated how the cross-sectional shape of the bluff body affects the energy conversion between the fluid and the body. While they found that a “T” shape had the greatest amplitude, it oscillated at a lower frequency than a cylinder, which led to it having a lower mechanical energy [16]. Therefore, a cylindrical shape best suits this application.

3.2.1 Preliminary Design

The preliminary design for the oscillating bluff body vortex energy harvester was composed of a cylindrical rod suspended within a duct by either one or two piezoelectric films.

The configuration in Figure 11 displays the rod suspended by two piezoelectric films. The cylindrical shape has been selected after consideration of the work done by Distler et. al. to determine the effect of bluff body shape on oscillation [18]. The cylindrical bluff body will oscillate normal to the flow due to the periodic lift force placed on the body as a result of Kármán Vortex Street generation. There will also be a periodic drag force on the bluff body, however this will be resisted by the orientation of the piezoelectric film.

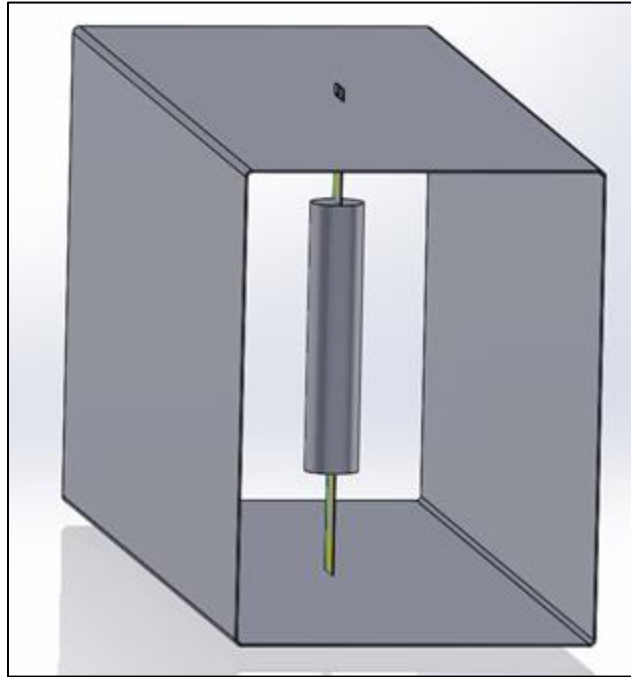


Figure 11: Preliminary Design for the Oscillating Bluff Body

The bluff body for this design is similar to that of the free end configuration of the Eel harvester. The key difference between the two is that the oscillating bluff body allows for one degree of freedom because of the piezo film bending, while the eel's bluff must be rigidly fixed. Modeling and simulation were therefore executed similarly to determine the optimal aspect ratio. As the ceramic piezoelectric will be fixed to the face of the duct and the oscillating cylinder, it can therefore be considered to be mass-dampened. This signifies that the natural frequency of the piezoelectric material will be much lower than if not dampened.

The group decided that two piezoelectric 'rods' should be used for the oscillating cylinder design. This decision was arrived at through research of similarly designed *VIVACE* systems. For example, the University of Michigan's largely successful (and larger scale) design uses a double connected system albeit with electromagnets rather than piezoelectrics. Past projects at WPI have used a single connected piezoelectric with unsuccessful results. It was also considered that the use of two piezoelectrics could make the system more stable (i.e. it should result in more uniform displacement across the cylindrical bluff body).

As the vortex shedding frequency primarily depends on the bluff body's characteristic length and velocity, the inlet flow velocity must be regulated to maintain a constant shedding frequency. Optimization was to be pursued in one of two directions. The first included designing

a nozzle with a variable area ratio. This nozzle would be designed to hit the target inlet velocity at the low end of the stream velocity range and decrease the area ratio with increased stream velocity. Conversely the nozzle could be designed to meet the target inlet velocity at the high end of the stream velocity range and increase the area ratio with decreased stream velocity. The second design direction would be to create a multiple-unit system, which is shown in Figure 12. This system would be set to operate at the low end of the stream velocity range. As velocity increases, a valve or flap will be opened due to the increased flow momentum allowing flow to pass through to a second unit in addition to the first. This process could then proceed for other units in the system. The performance of this multi-unit system would depend on the velocity ranges the units would be intended to operate on.

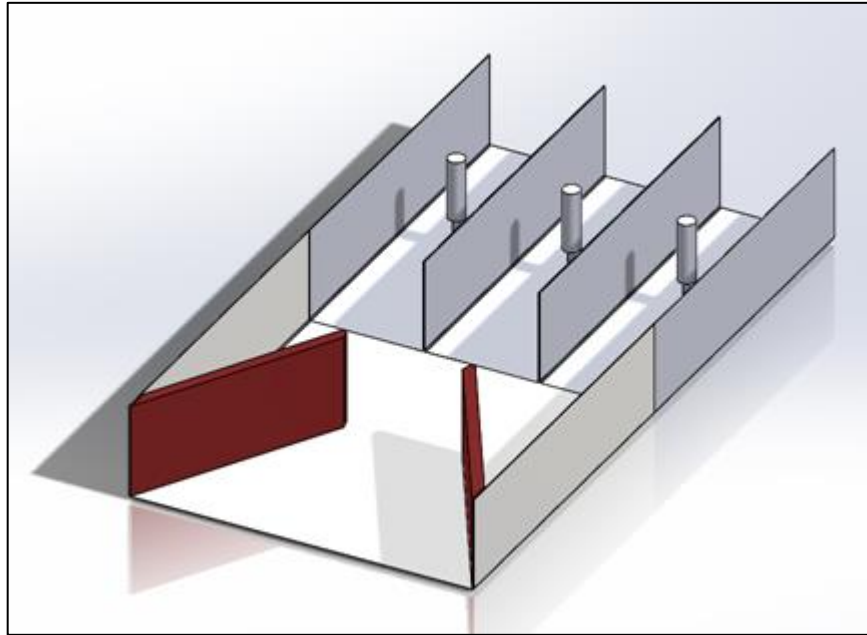


Figure 12: Preliminary Design of the Multi-Oscillating Bluff System

The nozzle design results discussed in section 3.2.4 ultimately showed that it would be significantly more difficult to regulate flow velocity to the bluff body from the free stream flow velocity than initially expected. However, the oscillating cylinder design optimization exceeds the capacity of what the team could achieve given the timeframe of the project.

3.2.2 Preliminary Calculations

The diameter of the bluff body is a function of the flow velocity, the intended vortex shedding frequency, and the Strouhal number which was approximated as 0.2. The initial expectation was to have a flow velocity within the duct of 5 m/s. The intended vortex shedding frequency depends on the piezoelectric material used; the ceramic piezo has an ideal frequency of 40 Hz when dampened. Equation 1 can be used to determine the initially estimated cylinder diameter of 2.5 cm.

The vertical length of the cylindrical bluff was found as a multiple of the bluff diameter. Determination of the optimal aspect ratio, which is the ratio of the cylinder height to diameter, is

explained in more detail in section 3.2.3. The duct dimensions can be found using the same case as for the suspended bluff configuration of the eel harvester. This results in a gap from the cylinder to the container of a quarter of the bluff body height. This may be altered due to the dimensions of available piezoelectric films. The duct width will be found using the same relation as for the eel harvester.

The lift force imposed on the cylinder by the flow can be characterized by Equation 9. This force causes the bluff body to oscillate normal to the flow. The amplitude of this oscillation can be modeled by the following equation:

$$Amplitude = \frac{\rho U^2 D L C_L}{2k * \sqrt{(1 - (\frac{\omega_s}{\omega_n})^2)^2 + (2\zeta \frac{\omega_s}{\omega_n})^2}} \quad (18)$$

Where omega (s) is the shedding frequency [radians], and omega (n) is the natural frequency of the piezoelectric material [radians]. D is the cylinder diameter, while L is the cylinder length, and k is the spring constant of the piezoelectric material. C_L is the lift coefficient from,

$$C_L = \frac{F_L}{\frac{1}{2} * \rho * U^2 D} \quad (19)$$

From the vortex shedding frequency, amplitude, and lift force the power output can be characterized as,

$$P = \frac{\omega_s \rho^2 U^4 D^2 L^2 C_L^2}{4k * \sqrt{(1 - (\frac{\omega_s}{\omega_n})^2)^2 + (2\zeta \frac{\omega_s}{\omega_n})^2}} \quad (20)$$

The remaining unknown dimensions are the length of the duct and the nozzle dimensions. Research has not found a numerical way to determine these dimensions, so they will be estimated and updated according to the simulations.

3.2.3 Preliminary Sketches/Drawings

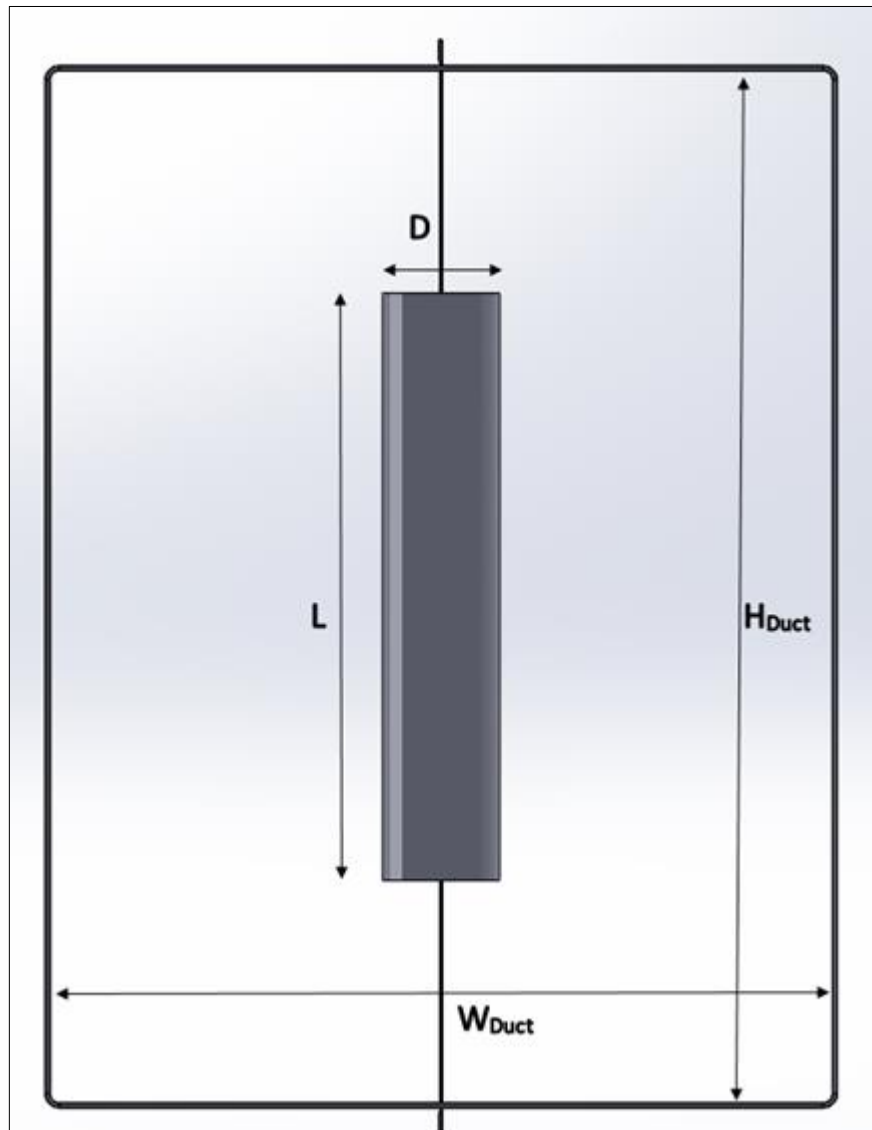


Figure 13: Preliminary Design of the Bluff Body within the Duct

3.2.4 Determining the Aspect Ratio

The aspect ratio for the oscillating bluff body was found similarly to that of the eel harvester configurations. Initially seven configurations were modeled in SOLIDWORKS with aspect ratios of 1 to 7. They were modeled to be contained by a simple rectangular pipe, thus enabling a 3D internal flow simulation around the bluff body to be used, as seen in Figure 14.

These simulations used the maximum free stream flow velocity multiplied by the increase from the nozzle, which were initially thought to be 2.5 m/s and 2x respectively, resulting in a uniform inlet velocity of 5m/s. This was then developed into a SOLIDWORKS simulation with the following characteristics:

- Boundary conditions of 5m/s at the inlet and environmental pressure (101 kPa) at the outlet.

- Rotational flow enabled.
- A sliding mesh over a time period of 1 second (To allow for transient analysis).
- A global mesh setting of 4
- A local refining mesh of 2 around the bluff body.

After running these studies, the transient analysis results were looked at to see if a vortex street was visible. Vortex street generation occurred down to an aspect ratio of 5. Verification of vortex street formation was accomplished by loading the transient analysis results and creating a cut plot along the plane perpendicular to the cylinder and at the center of its height. The velocity streamlines were selected to be shown and the pressure distribution was also shown for further insight. Examples of these cut plots can be seen in the two figures below, each displaying the aspect ratio of 5 configuration at two different simulation times:

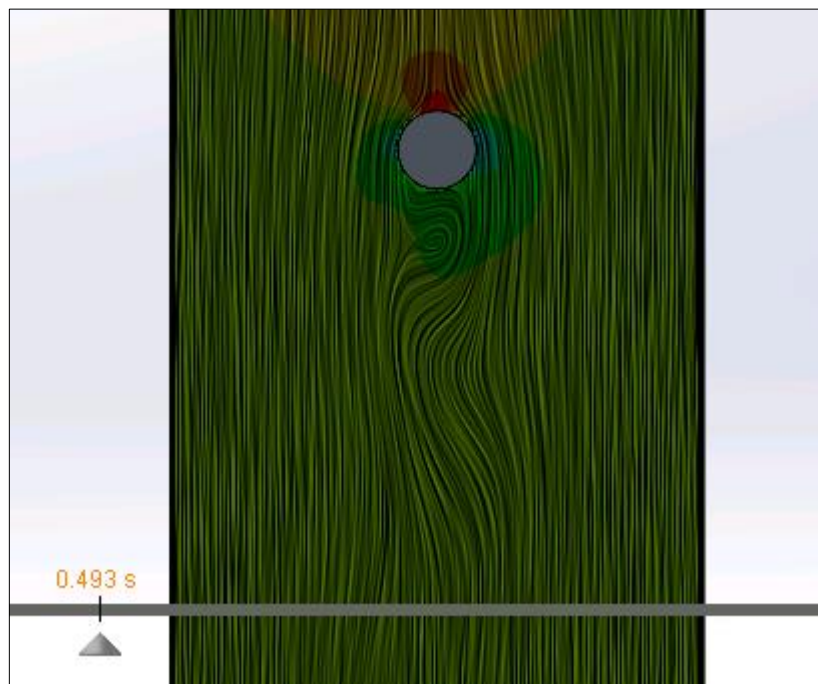


Figure 14: Vortex Street at 0.493 seconds for an Aspect Ratio of 5

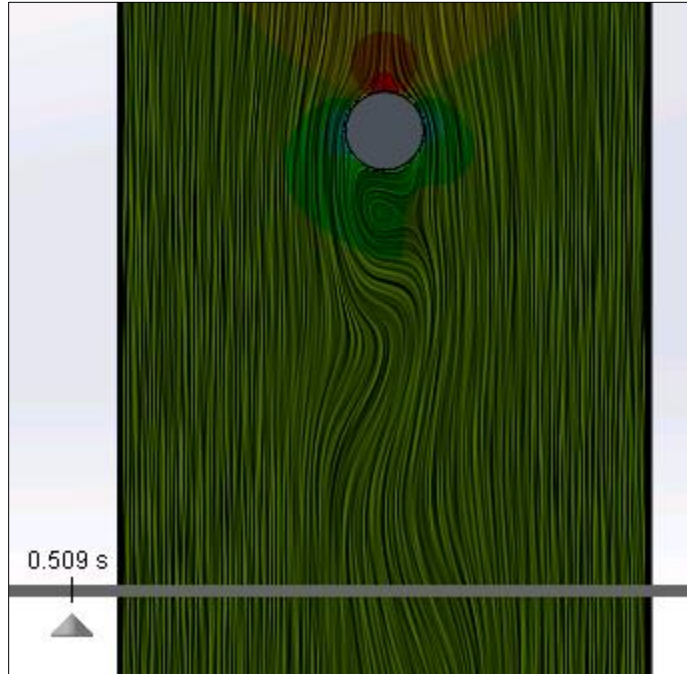


Figure 15: Vortex Street at 0.509 Seconds for an Aspect Ratio of 5

The findings from the nozzle design in Section 3.3 show a nozzle velocity increase of 1.5 times the free stream velocity. It was also determined that it would be best to pursue an oscillating bluff design that reached peak efficiency at the median of the flow range, 1.5 m/s. Therefore, the bluff body's necessary diameter was recalculated the using a flow velocity of 2.25 m/s (1.5 x 1.5 m/s). This returned a diameter of 4.4in.

The flow simulations were then run again using the same settings as above, however with an inlet flow velocity of 2.25 m/s. Once again, an aspect ratio of 5 was found to be the lowest ratio that exhibited vortex street generation.

3.2.5 Force Analysis

To better assess the dynamics of the oscillating bluff, another flow simulation was run to determine whether the system would oscillate as intended. This was accomplished by performing a SOLIDWORKS force analysis from the pressure distributions on the cylindrical bluff body and the piezoelectric rods. A *split line* was used in the model so both halves (facing each of the container walls) of the cylinder could be analyzed for pressures and forces. This analysis was performed to assess how well the lift forces oscillated according to expectation, as well as whether the pressures on the piezoelectric films would hinder performance.

The flow simulation was run for aspect ratios 5, 6, and 7. The simulation characteristics remained the same except for the following changes:

- A sliding mesh over a time period of 1.5 seconds, set to save from 0.5 sec to 1.5 sec at 0.75 sec intervals.
- A global mesh of 3.
- A local refining mesh of 4 around the bluff body.

The pressure and force experienced by each face of the cylinder bluff and both piezoelectric films, for each time increment, were exported to excel. Table 1 displays the net forces in the positive direction on the cylinder, the piezoelectric films, and in total:

Table 1: The Forces on the Cylinder

Physical Time	Net Positive Cylinder	Net Positive Piezo	Net Positive System
[sec]	[N]	[N]	[N]
0.5	0.090	0.099	0.189
0.575	-0.001	0.106	0.105
0.65	0.015	0.075	0.091
0.725	0.002	0.103	0.104
0.8	0.010	0.085	0.095
0.875	0.034	0.118	0.152
0.95	-0.009	0.084	0.075
1.025	0.040	0.105	0.145
1.1	-0.026	0.086	0.060
1.175	0.061	0.105	0.166
1.25	-0.053	0.089	0.036
1.325	0.099	0.112	0.210
1.4	-0.063	0.093	0.030
1.475	0.083	0.099	0.182
1.5	0.064	0.090	0.154
	Minimum	Minimum	Minimum
	-0.063	0.075	0.030
	Maximum	Maximum	Maximum
	0.099	0.118	0.210

It can be seen from the *Net Positive Cylinder* results (the net force in the positive X direction from the simulation) that the desired oscillating lift force is present. The results from *Net Positive Piezo* highlight the potential interference the piezoelectric rod may have on the performance of the system. This is likely due to the comparable surface area of the rods compared to that of the bluff body. The *Net Positive System* results show that there will be an oscillation of force on the cylinder, however not an oscillation with peaks in opposite directions.

It is important to note that this is solely an analysis of the total amount of force on the faces of the system. These bulk forces will not have as great an effect on the motion of the system as the moments relative to the fixed ends of the piezo rods will have. Therefore, the full forces on the piezo rods will not have as great an effect on the motion of the system as may appear from the above results.

Another observation from these results is that an increase in the surface area of the cylinder bluff body relative to those of the piezo rods will decrease any interference from the rods and better enable the desired motion to occur. Therefore, use of smaller piezo rods, or a

direct increase in the surface area of the bluff body, whether by an increase in the aspect ratio or by an increase in diameter (i.e. in the case of use for a greater flow velocity), could enable better expected results than those simulated.

3.3 Eel Harvester Design

The piezo-film method utilizes a fixed, rigid bluff body and a flexible film. The film, located sufficiently downstream of the bluff body will act similar to a flag waving in the wind. The periodic vortices shed by the bluff body will impact the flexible film, causing it to strain in an oscillatory fashion. A mechanism was designed to dynamically adjust the bluff body size to control the vortex generation frequency with changes in flow speed.

3.3.1 Preliminary Eel Harvester Design

The preliminary design for the “Eel” vortex energy harvester consisted of the two configurations shown below in Figure 11. The two configurations were similar, each having a piezoelectric film behind a variable-width bluff body plate within a rectangular duct. The variable width plate is positioned in front of the piezoelectric film to create the Kármán Vortex Street to bend the piezoelectric film. In front of the duct is a nozzle to increase the flow velocity in the duct and around the plate, shown below in Figure 16.

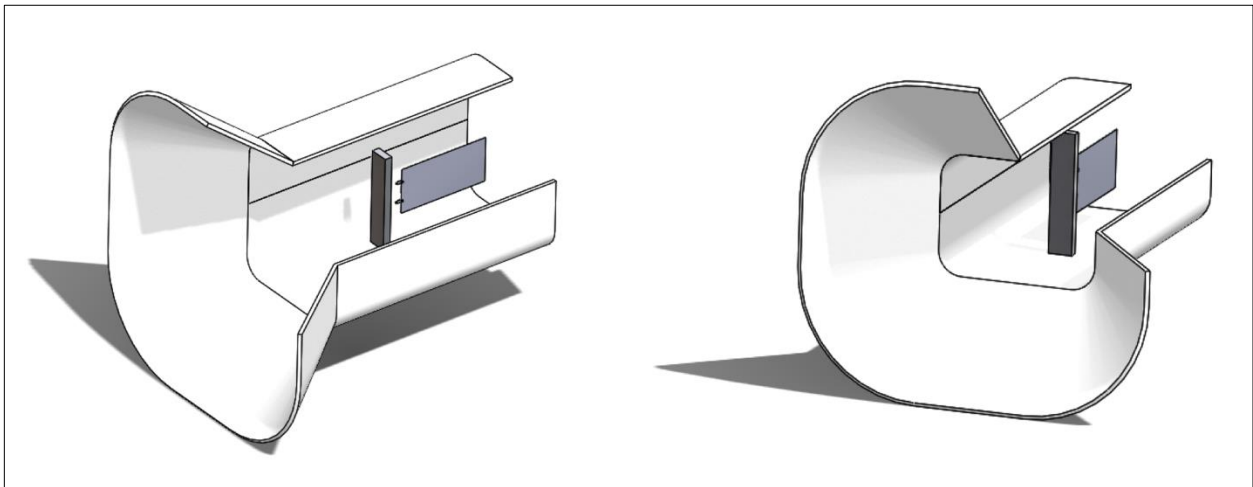


Figure 16: 16a (left)/16b (right), Preliminary Designs for the "Eel" Harvester

The left picture of Figure 16a shows the “free end” configuration, where the bluff body plate is spaced between the top and bottom of the duct to allow flow over the top of the plate. Figure 16b shows the “fixed end” configuration where the top and bottom of the plate are connected to the duct. The free end configuration would create a higher vortex shedding frequency but the street would rotate around the bluff body [11] while the fixed end would be consistently shedding in the same orientation. Both configurations were examined via simulation to determine which would produce the more optimal physical results.

To control the shedding frequency despite variations in flow speed, the width of the plate is controlled by another body placed in the flow upstream from the plate. When the velocity of the flow increases, the momentum flow causes the pad to move. The displacement of the pad causes a mechanism to contract or expand the bluff body. We are able to predict what the length of the bluff body should be based on the Strouhal Number and momentum flow rate equations.

3.3.2 Preliminary Calculations

The duct width was found using a study on various blockage percentages of ducts and their effects on vortex street generation. It concluded that blockage percentages over 10% required adjustments in the vortex street generation calculations due to the fluid acceleration from the blockage [25]. To ensure that neither configuration goes above this critical value, the width of the duct will be:

$$W_D = \frac{1}{0.10} * L_{max} \quad (21)$$

The height of the duct will vary between the two configurations. The aspect ratio (AR) has been found from previous research to cause the vortex street axis to rotate around a square flat plate bluff body when AR=1, with diminished rotation as the aspect ratio increases [14]. This means that parametric simulations were needed to determine at what point this rotation became negligible. The free end configuration will be increased by the distance between the buffer and the wall. Through research, it was found that when the gap is a quarter of the height of the bluff body the Strouhal number will be at a maximum. This gives a height for the free ends configuration of:

$$H_D = 1.5 * AR * L_{max} \quad (22)$$

For the bluff body attached to the wall, a height of:

$$H_D = AR * L_{max} \quad (23)$$

Using the momentum flow rate, the front face of the body would be perpendicular to the flow direction, and that the drag would be assumed to be negligible.

For momentum flow rate:

$$\frac{1}{2} * \rho * U_{\infty}^2 * A_c = \frac{St * f}{L_{max}} \quad (24)$$

Since the drag coefficient is a function of the Reynolds number, if it cannot be assumed to be negligible then a more complicated mechanism to relate the fluid velocity to the maximum width of the bluff body would be required. We had initially planned on manufacturing and testing the mechanism with the completed nozzle design to determine if the drag could be assumed to be negligible. This could have been figured out by comparing a measured change in the bluff body to the predicted change. The size of what we could manufacture was limited by

the manufacturing processes available to us, leaving us unable to make a testable variable bluff body mechanism.

The remaining unknown dimensions are the distance from the bluff body to the piezoelectric material, the length of the duct, and the nozzle dimensions. Research has not found an analytical method of determining these dimensions, so they will be estimated and updated according to additional simulations. The film will be placed close enough to the buffer to be inside the vortex street, but far enough away not to suppress the vortex street generation.

3.3.3 Preliminary Sketches/Drawings

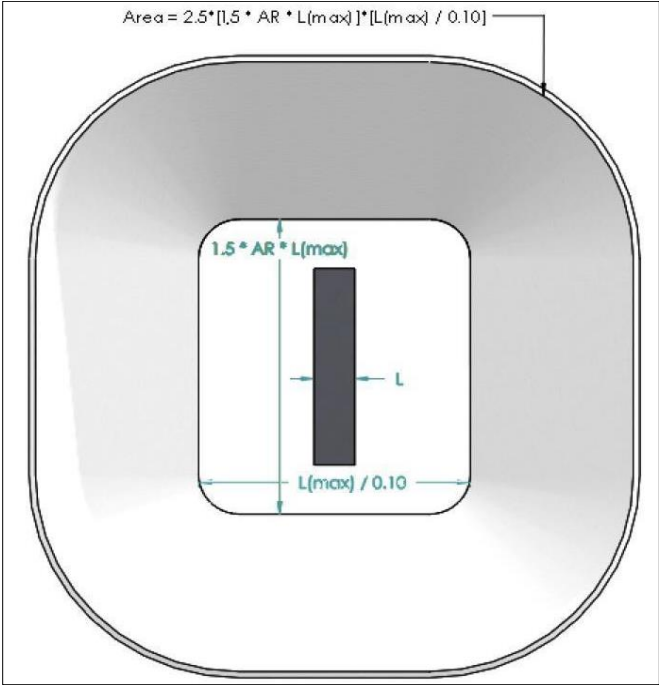


Figure 17: Front View of the Free End Configuration

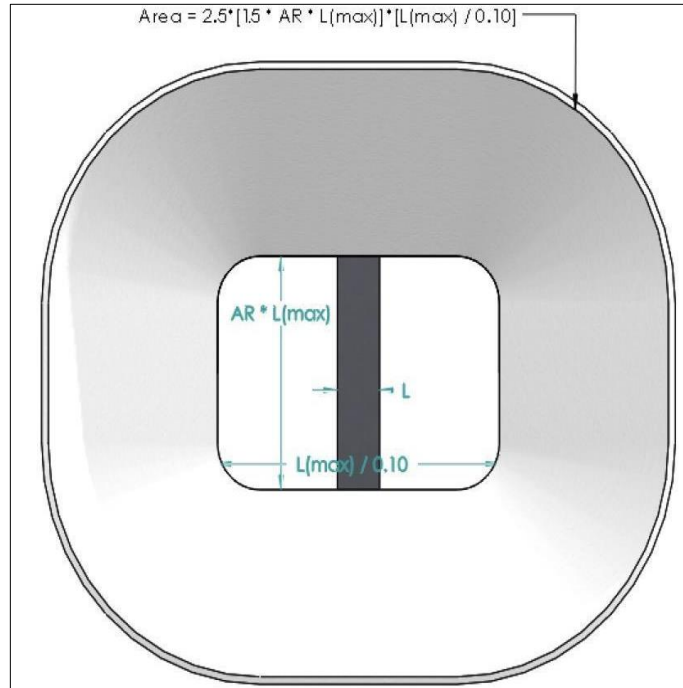


Figure 18: Front View of the Fixed End Configuration

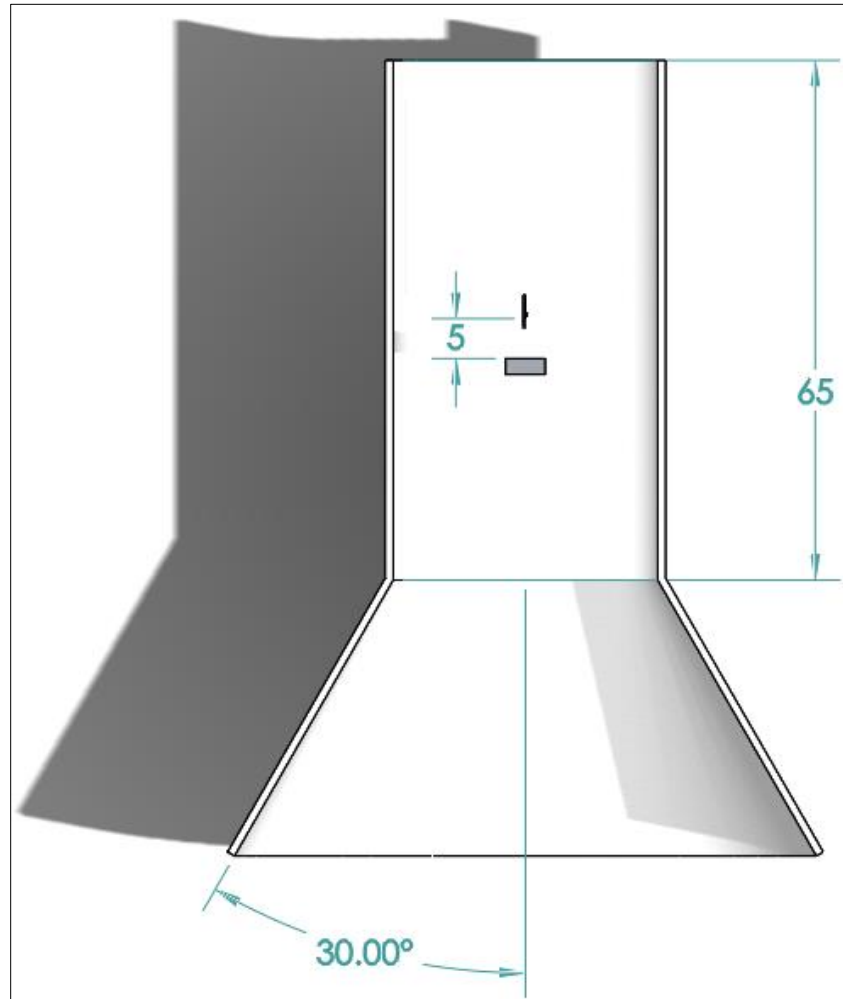


Figure 19: Cross-Section Top View

3.3.4 Flow Simulations to Revise Nozzle Design

To validate the assumptions of the initial nozzle design, fluid flow simulations were developed and performed using the SOLIDWORKS Flow Simulation software package. For the first nozzle simulation, an external study was performed with the following characteristics:

- General mesh size of 2.
- Local mesh size of 2, enveloping the entire nozzle.
- Ambient atmospheric pressure (101kPa).
- Initial inlet flow speeds of 0.5m/s, 1m/s, and 2 m/s.

These tests showed no increase in speed within the nozzle. This was determined to be due to the lack of a decrease in pressure after the converging section of the nozzle, the water flowed around the high pressure convergent section.

To address this, the nozzle was redesigned to include a divergent section immediately after the bluff body, with a revised goal of increasing the flow velocity in the nozzle by 1.5 times the inlet velocity. This is shown below in Figure 15.

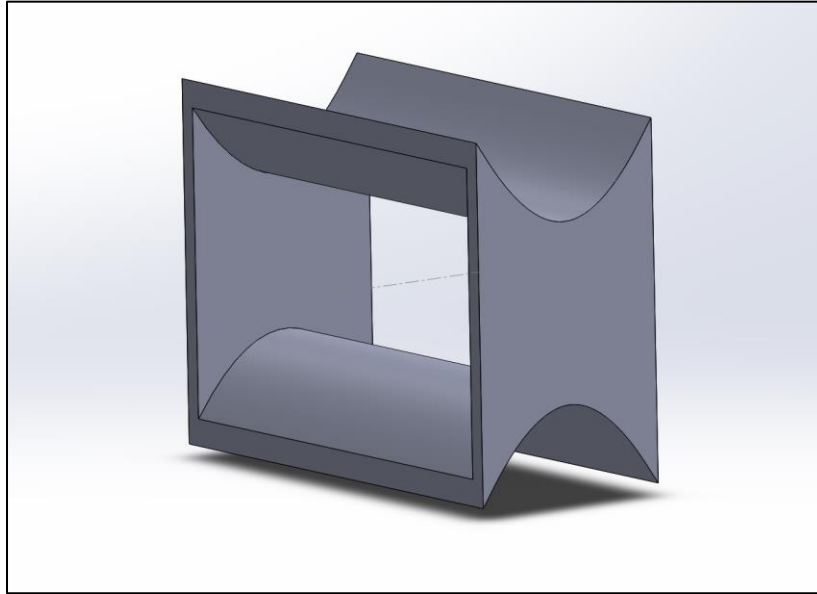


Figure 20: The Redesigned Nozzle

To determine the optimal length, width, and height of the nozzle, another SOLIDWORKS Flow Simulation study was used to maximize the flow speed in the center of the nozzle. This was done as a 3D external flow study with the following characteristics:

- An inlet velocity of 1 m/s going into the nozzle, ambient atmospheric pressure, 15 total iterations.
- Varying the height from 33.3mm < value < 66.7mm
- Varying the length 30mm < value < 60mm.
- Varying the width at four values, 30mm, 40mm, 50mm, and 60mm.
- A general mesh setting of 4.
- A local mesh around the entire nozzle with a refining mesh of 3.

This study created 15 different configurations with combinations of these dimensions. It showed the greatest velocity increase with values of 60mm, 61mm, and 57mm for the length, width, and height respectively. Since this was a rough run with only 15 iterations for three variables, we then ran two 2D external parametric studies to give more accurate numbers. The first one was performed with the following characteristics:

- An inlet velocity of 1 m/s entering the nozzle, ambient atmospheric pressure, 16 different iterations.
- A constant nozzle width of 33.33mm.
- Varying the nozzle height at four values: 41.67mm, 45mm, 50mm, and 55mm.
- Varying the nozzle length at four values: 53mm, 55mm, 57mm, and 59mm.
- A global mesh setting of 3
- A local mesh around the nozzle with a refining mesh of 5.

The first 2D external parametric study produced the following results, the highest values are highlighted in yellow:

Table 2: The results of the first 2D parametric study

Design Point	Length (m)	Width (m)	Velocity (m/s)
1	0.053	0.04167	1.076
2	0.053	0.045	1.050
3	0.053	0.05	1.097
4	0.053	0.055	1.112
5	0.055	0.04167	1.071
6	0.055	0.045	1.061
7	0.055	0.05	1.113
8	0.055	0.055	1.105
9	0.057	0.04167	1.059
10	0.057	0.045	1.072
11	0.057	0.05	1.123
12	0.057	0.055	1.114
13	0.059	0.04167	1.070
14	0.059	0.045	1.065
15	0.059	0.05	1.125
16	0.059	0.055	1.120

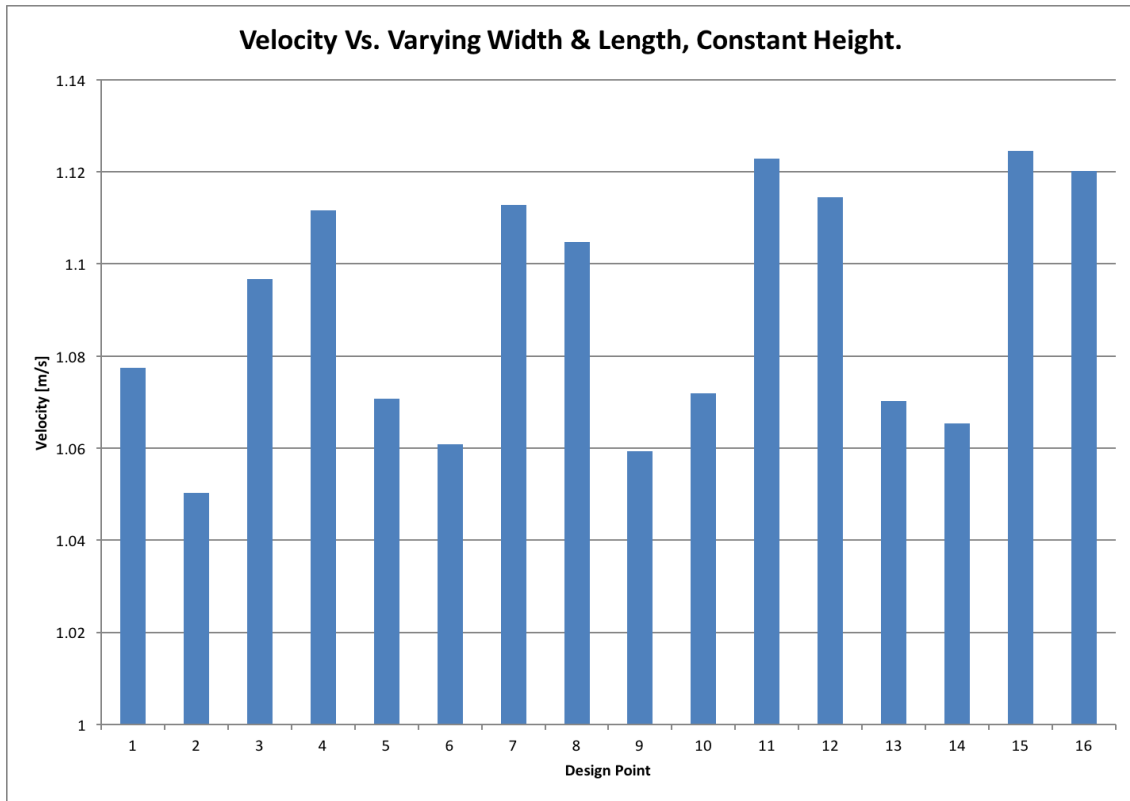


Figure 21: A graphical representation of the first parametric study results.

The second parametric 2D external study was then performed with the following characteristics:

- An inlet velocity of 1 m/s going into the nozzle, ambient environmental pressure, 20 total iterations.
- A constant width of 41.67mm.
- Varying the height at five values: 33.3mm, 44.4mm, 55.5mm, 66.6mm, and 77.7mm.
- Varying the length at four values: 53mm, 55mm, 57mm, and 59mm.
- A general mesh setting of 3
- A local mesh around the nozzle with a refining mesh of 5.

The width was not varied in the second study since it did not seem to increase the flow speed nearly as much as increasing the length or height did. The velocity of the flow at the center of the nozzle is shown below in Table 3. The highest values are highlighted in yellow:

Table 3: The results of the second 2D parametric study.

Design Point	Length (m)	Width (m)	Velocity (m/s)
1	0.053	0.033	1.206
2	0.053	0.044	1.318
3	0.053	0.056	1.238
4	0.053	0.067	1.259
5	0.053	0.078	1.269
6	0.055	0.033	1.181
7	0.055	0.044	1.336
8	0.055	0.056	1.242
9	0.055	0.067	1.249
10	0.055	0.078	1.264
11	0.057	0.033	1.195
12	0.057	0.044	1.345
13	0.057	0.056	1.248
14	0.057	0.067	1.279
15	0.057	0.078	1.285
16	0.059	0.033	1.207
17	0.059	0.044	1.348
18	0.059	0.056	1.263
19	0.059	0.067	1.283
20	0.059	0.078	1.302

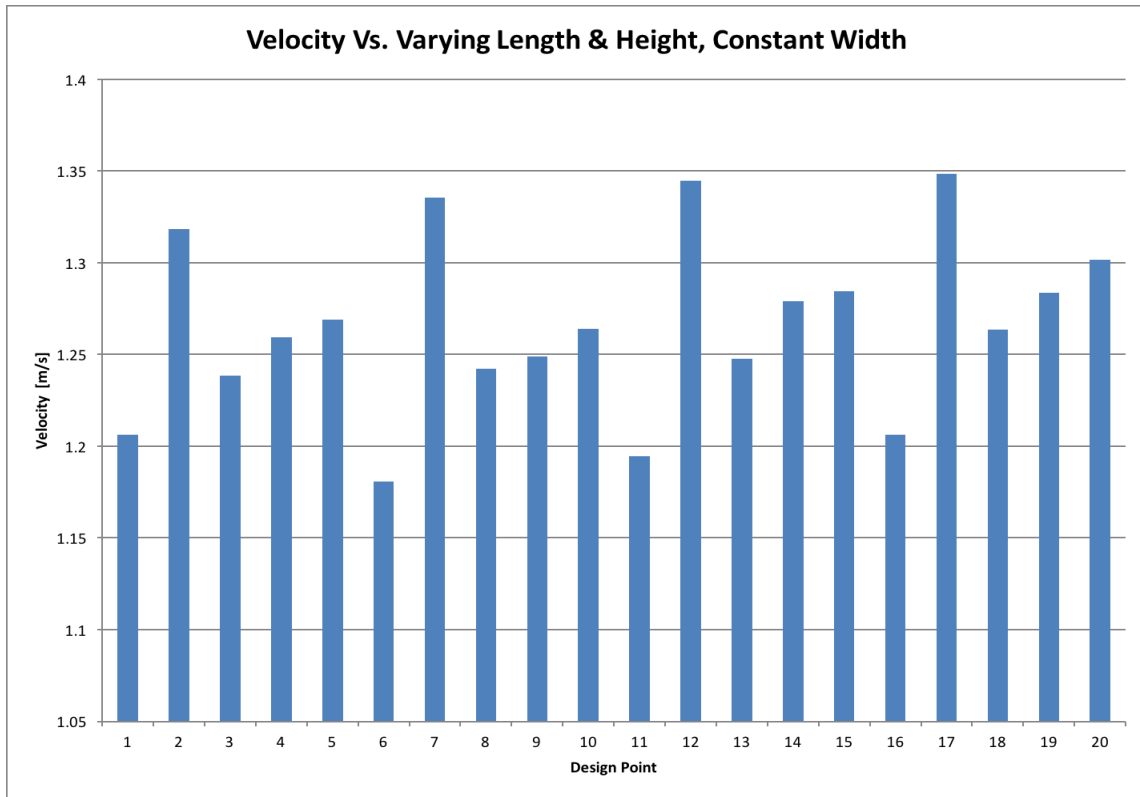


Figure 22: A graphical representation of the second parametric study results.

From this comparison, optimized nozzle dimensions of 59mm, 44mm, and 50mm were chosen for the length, width, and height respectively.

These results appeared to show unexpected vortex street forming around the nozzle in the external flow study, shown in Figure 18 below. At first it was questioned whether it was due to an issue with the meshing of the model. To verify this, the mesh was increased to the largest value where the simulation could still complete the study within a reasonable timeframe, which resulted in the use of a global mesh of 4 and local refining mesh of 3. With these settings a vortex street still appeared to be developing around the nozzle. It was determined that despite its existence, that particular street would not be a large concern as it did not appear to affect the flow within the nozzle. However, it is worth noting its existence (Figure 23).

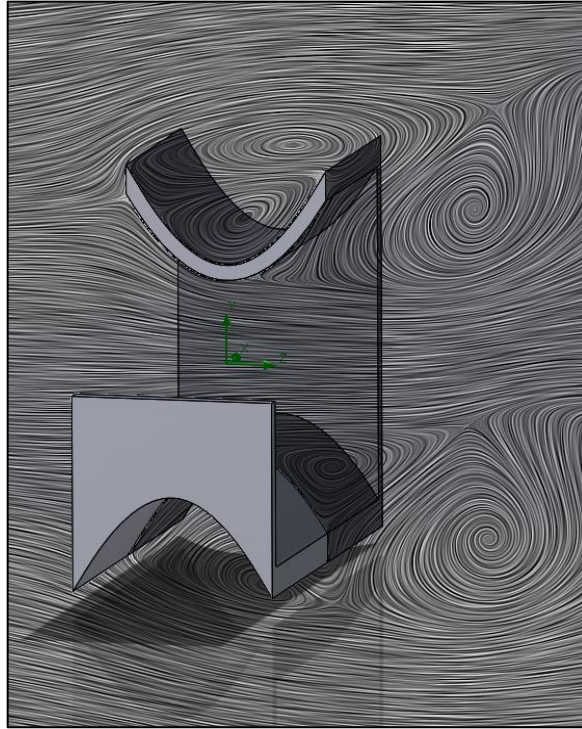


Figure 23: Evidence of the Nozzle Generating Vortices.

Measuring from a point at the middle of the nozzle's vertical centerline, this nozzle design appears to increase the average flow speed inside of the nozzle by an average of approximately 1.5 times in the 2D simulations. As a 3D simulation is not feasible due to time and computational resource requirements, this result will be need to be verified experimentally.

3.3.5 Determining the Redesigned Nozzle Aspect Ratio

The aspect ratios for the free end and fixed end configurations were found the same way. Initially seven configurations were created with aspect ratios of 1 to 7, which were modeled in SOLIDWORKS as a simple rectangular pipe with a 4.167mm bluff body in the middle. A 3D internal flow simulation was then developed where the inlet is at the far right and the outlet is at the far left. The simulation setup is shown below in Figure 19.

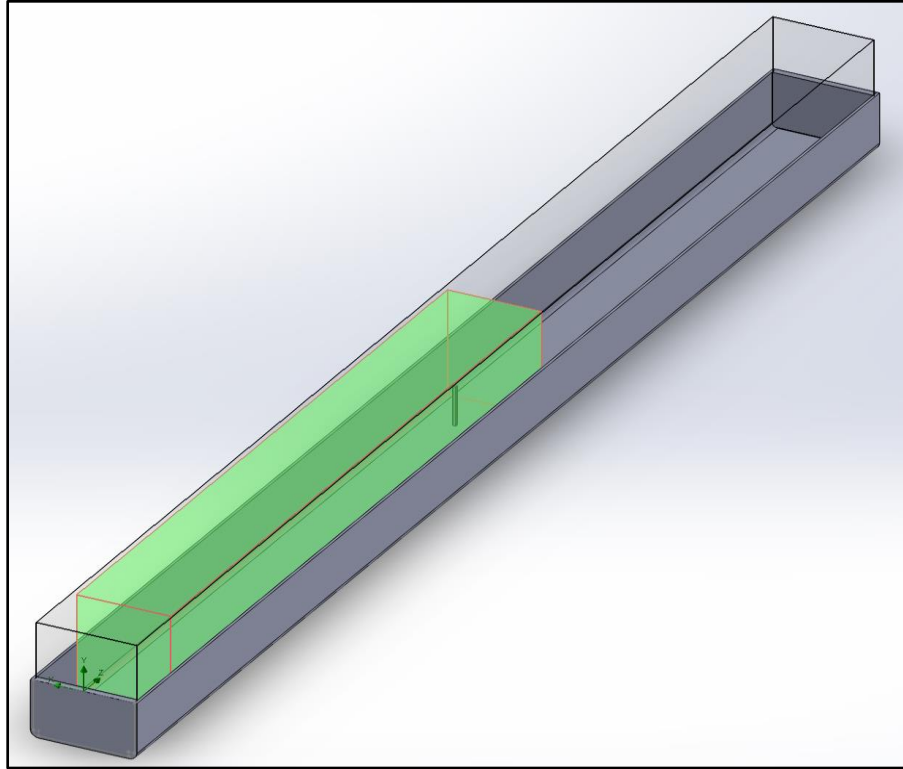


Figure 24: SOLIDWORKS Flow Simulation Setup for Determining Aspect Ratio.

These simulations used the maximum free stream flow velocity multiplied by the increase from the nozzle, which were initially thought would be 2.5 m/s and 2 times respectively, resulting in a uniform inlet velocity of 5m/s. These SOLIDWORKS simulations had the following characteristics:

- Boundary conditions of 5m/s at the inlet and environmental pressure (101kPa) at the outlet.
- Rotational flow enabled.
- A sliding mesh over a time period of 1 second (To allow for transient analysis).
- A global mesh of 4
- A local refining mesh of 2 around the bluff body.

After running these studies, the transient analysis results were looked at to see if a visible vortex street developed, shown in Figure 20. For the free end configuration, vortex street generation happened from 7 down to an aspect ratio of 5, but for the wall end configuration this happened from 7 down to an aspect ratio of 3. For the wall end configuration, a final aspect ratio of 4 was chosen due to size limitations concerning the ability for the piezoelectric eel to have clearance in the nozzle.

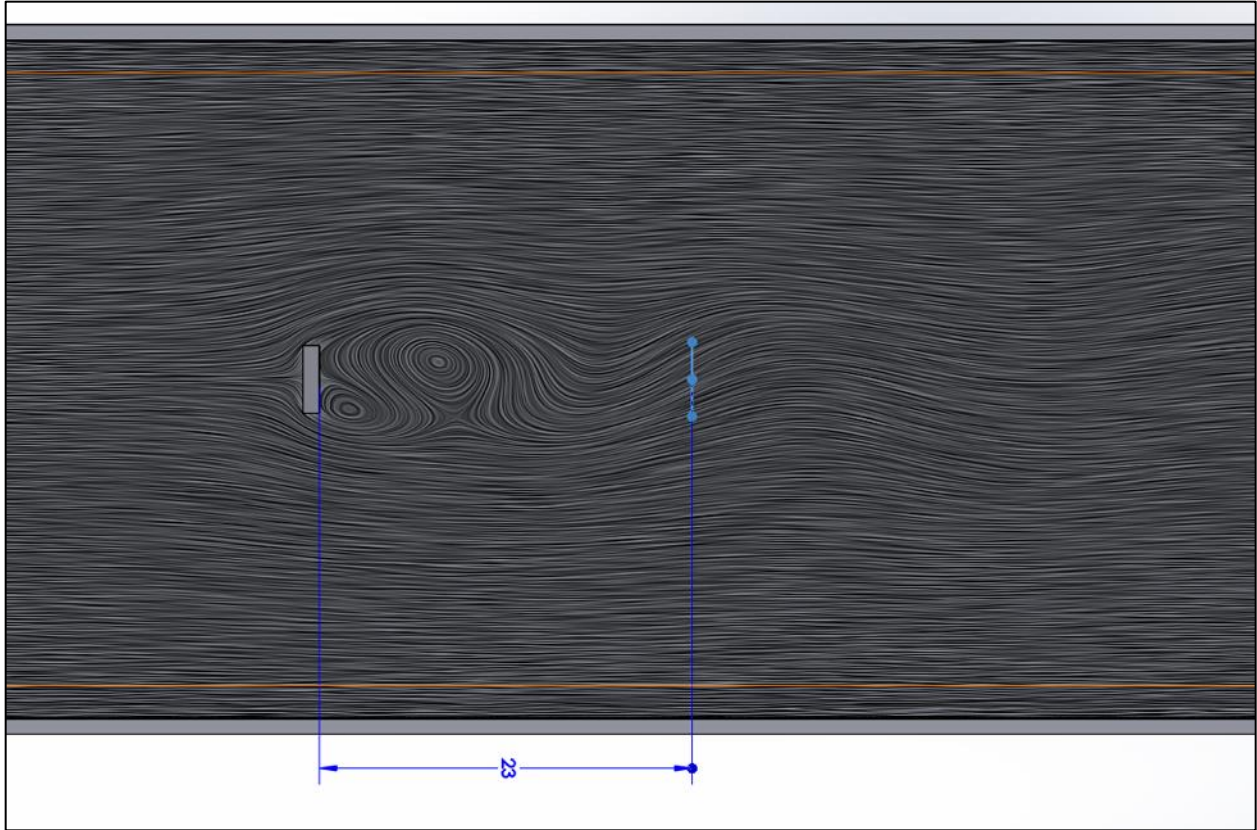


Figure 25: Vortex Street Generation Shown for Fixed End Configuration, Aspect Ratio 4.

Once it was determined that the initial nozzle design would not reach the desired 2x nozzle velocity increase, the aspect ratio simulations were performed again for aspect ratios varying from 3 to 5 with the new desired velocity increase of 1.5x. All three simulations showed vortex street generation, so an aspect ratio of 4 was selected, as it would still be the smallest aspect ratio that was large enough not to block the flow over the piezo. At this aspect ratio, the bluff body diameter was 4.167mm, which would then be used as the starting point for determining the minimum bluff body diameter.

The free end configuration would require a larger nozzle than the wall ends configuration, which would be less-desirable for small applications, like powering a remote sensor. Additionally, attaching the mechanism to vary the size of the bluff body would be more difficult. As a result, the wall ends configuration was chosen for the final design.

3.3.6 Determining the Minimum Bluff Body Diameter

The last step for finalizing the nozzle design was to determine the minimum diameter that would be suitable for vortex street generation. Once the aspect ratio of 4 was finalized, determining the minimum diameter was a matter of running additional fluid flow simulations at the lowest stable free stream velocity, and lowering the bluff body size from 4.167mm until the vortex street did not fully engulf the piezo. Similar to Figure 24, this was modeled as a fluid flow

simulation within a rectangular tube. In this case, the inlet flow is from the left side, the outlet is on the right, and the bluff body is in the middle.

This simulation was developed and run with the following characteristics:

- Inlet velocity set to 0.75 m/s, outlet set to atmospheric pressure (101 kPa)
- Bluff bodies with 2mm thickness, 16.66mm height, and characteristic lengths of 4.167mm, 2.58mm, 2.33mm, 2.08mm, 1.79mm, 1.54mm, and 1.29mm.
- Transient analysis for a period of 1 second.
- Global mesh set to 4.
- Local refining mesh set to 3.

For each bluff body diameter, a top-down view of the vortex street generation transient, such as the one shown in Figure 20 was analyzed. Specifically, the pictures were analyzed to determine if a visible vortex street had developed, as well as the quantitative effective distance that the piezoelectric film could be placed within the street and still be affected. The results of these simulations in Table 4 showed that the possible minimum diameter would be around 1.5mm in width.

Table 4: Results of the Minimum Diameter Simulations

Bluff Body Size	Usable Vortex Street Generated?	Vortex Street Effective Distance
4.167mm	Yes	25mm
2.58mm	Yes	25mm
2.33mm	Yes	23mm
2.08mm	Yes	23mm
1.79mm	Yes	21mm
1.54mm	Yes	21mm
1.29mm	No	5mm
1.04mm	No	5mm

3.3.7 Final Eel Nozzle Design

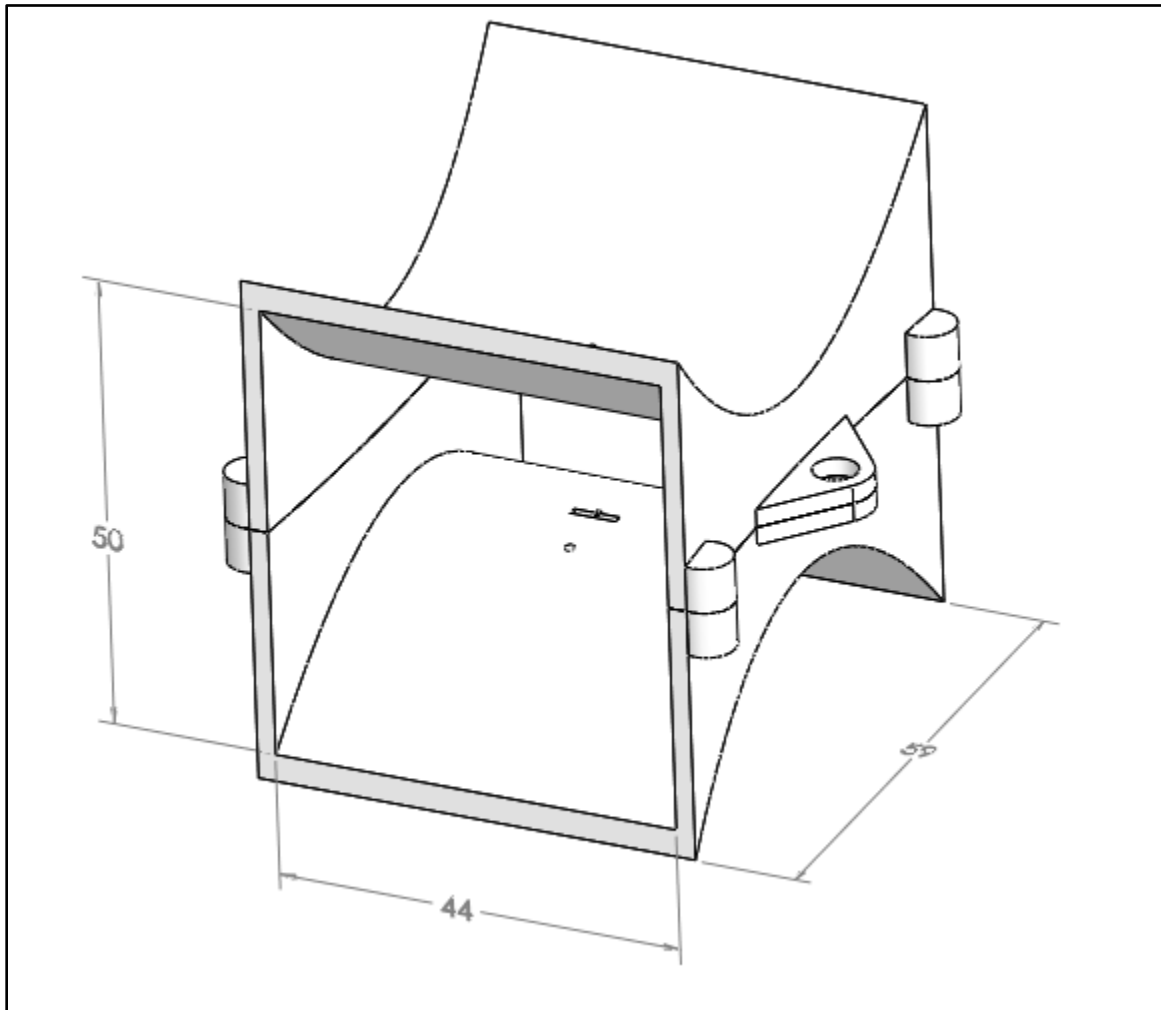


Figure 26: Final Nozzle Design

After the dimensions to the nozzle were updated based on the flow simulations, the model was further modified so that it could be manufactured easily. It was broken into two halves to make it easier to 3D print and assemble. Two slots were added so that the bluff bodies could be inserted in through the top to facilitate the exchange of bluff bodies during testing. The slot on the top of the nozzle goes all the way through, while on the bottom the slot only goes partially through the material so that the bluff body will not slide out of the bottom piece of the nozzle during testing. Additionally, there is a notch at the center of these slits so that a small extrusion on the center of the bluff body will always be lined up with the center of the nozzle to keep it from moving horizontally.

Two small holes were added behind the slots for the bluff body that will be used to run the lead wires through to the piezo. The first test will be conducted by suspending the piezo by its lead wires, such that it is supported similar to a flag in the vortex street.

To connect the two halves of the nozzle, four holes were added to the corners on both pieces such that 6mm long, 1/8" aluminum rods could connect and align the two halves. Additionally, two holes for 3/16" nuts and bolts were also added so the two halves could be connected together. These bolts were then used to attach the nozzle to part of the testing rig so it could be easily suspended underwater during testing.

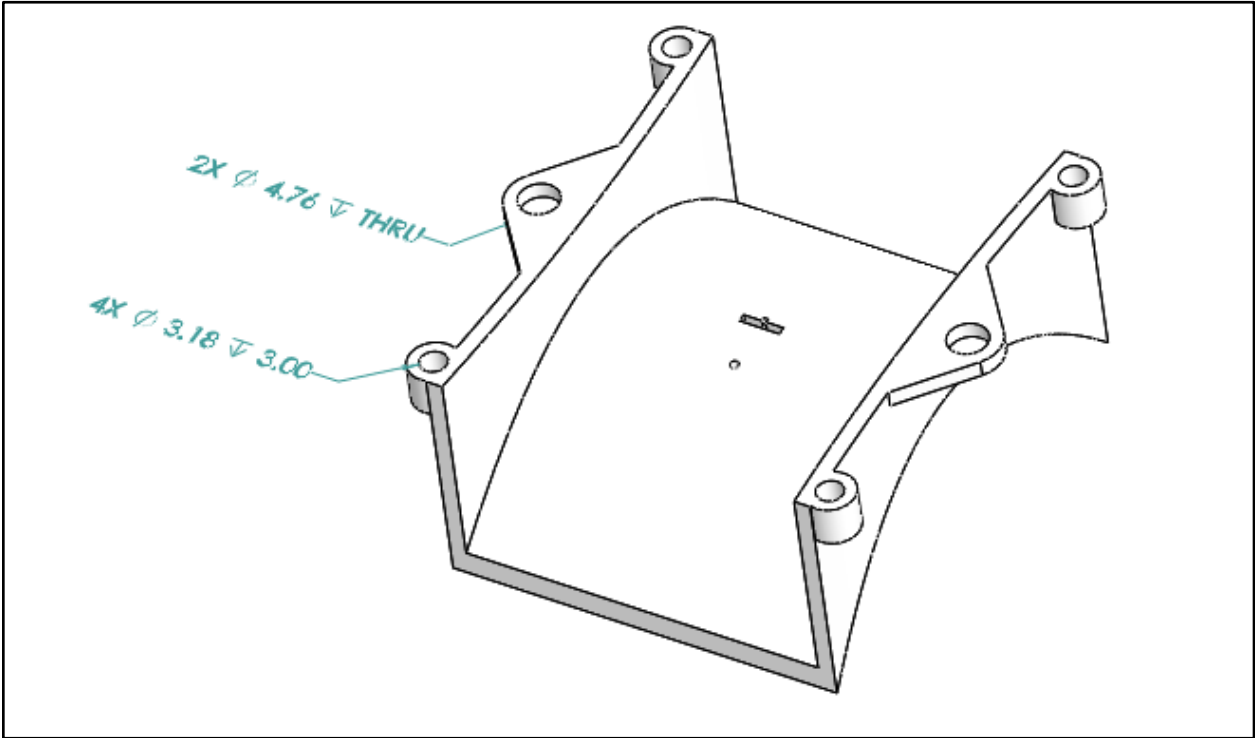


Figure 27: Bottom Piece of the Nozzle

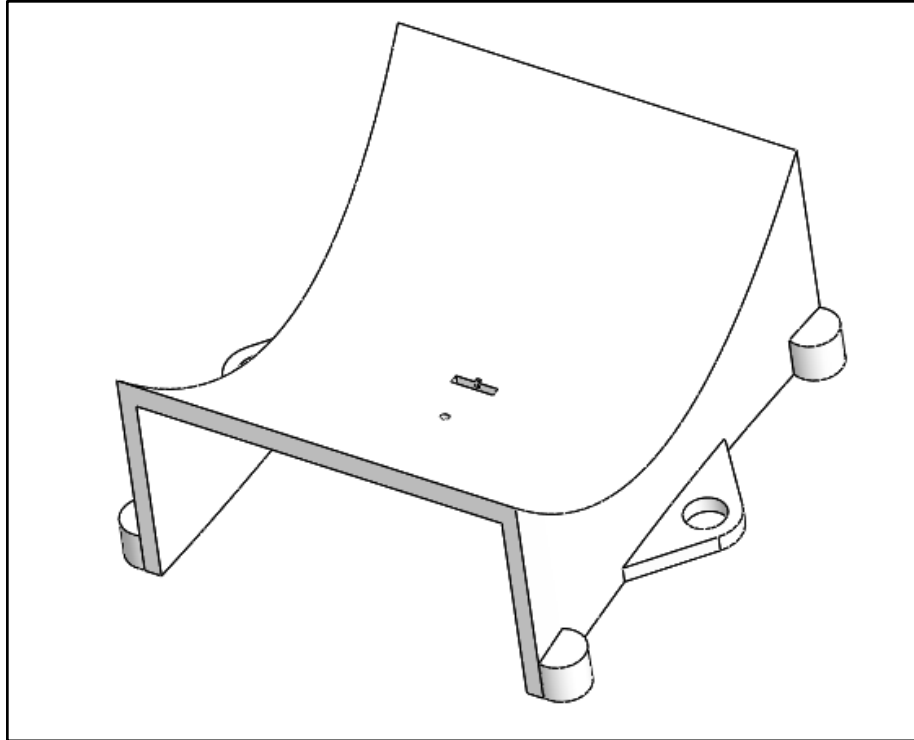


Figure 28: Top Piece of the Nozzle

3.4 Bluff Body Mechanism Design

In order to vary the size of the bluff body, we designed a mechanism (Figure 29) to relate the momentum flow rate from the free stream velocity to the water velocity inside of the nozzle. This device would be attached to the top and bottom of the nozzle, so that one controls half the change in size of the bluff body. It consists of six parts, a pad that is perpendicular to the flow, a disc with a varying radius, rod that gets displaced by the disc, a base, and two springs. As shown above, a gear will spin the disc as the pad gets displaced. This displacement will happen if the free stream velocity changes, as the force balance with the large spring will change. Rotating the disc will either push out the rod that is attached to the bluff body, pulling the bluff body outwards, or the small spring will push the rod in, making the bluff body smaller.

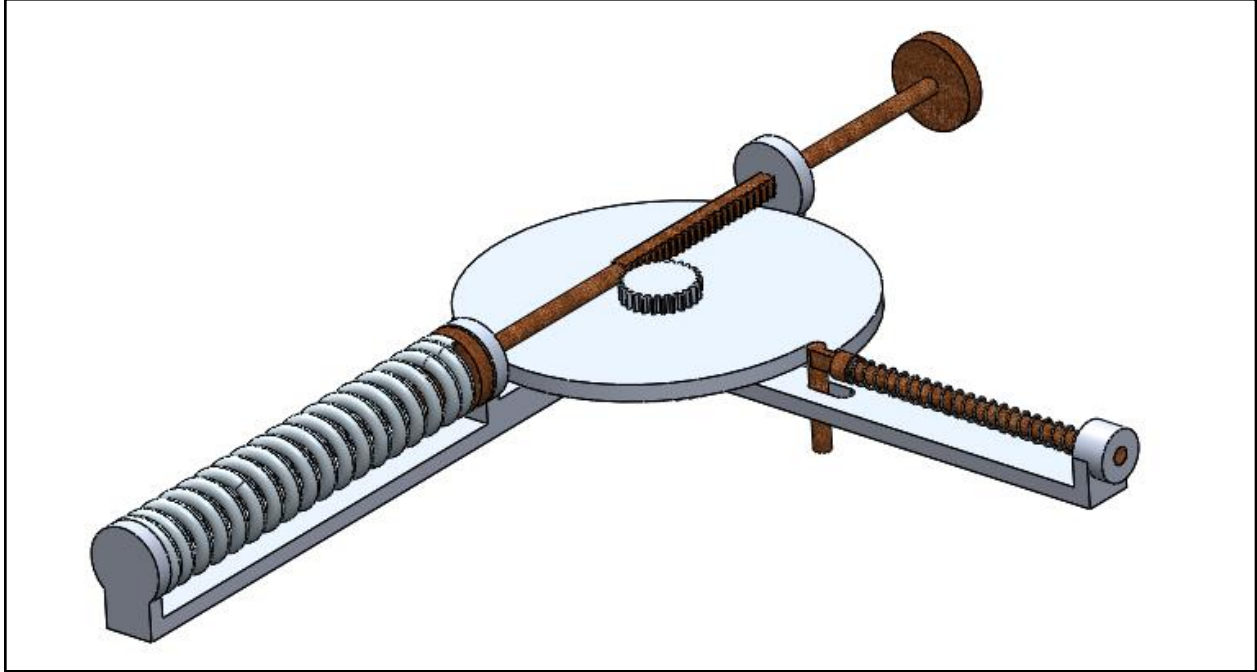


Figure 29: Mechanism to Change the Bluff Body Length based on Flow Speed

To determine the size of the components, as well as the shape of the disc, we used a MATLAB script that solves force balance between the water of the pad, the large spring, the small spring, and the frictional forces using two predetermined springs. The specific parts are explained below and the script can be found in Appendix A.

The MATLAB script runs a “for loop” function that varies the value PR , the extent of disc rotation. It uses two commercially sourced springs, a strong one with a spring constant of 5.1976 N/m, and a maximum deflection of 0.0125 m, and a weak one with a spring constant of 0.0734 N/m. From the strong spring constant and maximum deflection, the weight and the area of the pad are found using the two spring deflection equations below, where only one has a deflection:

$$\begin{aligned} Def * K_1 &= 0.5 * p * U_f^2 * A - W * K_f \\ 0 &= 0.5 * p * U_i^2 * A - W * K_f \end{aligned} \quad (25 \ \& \ 26)$$

Where Def is the deflection of the strong spring, K_1 is the spring constant for the strong spring, U_f is the maximum fluid velocity, and U_i is the fluid velocity at which the size of the bluff body will begin to change, W is the weight of the rod, K_f is the friction coefficient between the rod and the base, and A is the area at the beginning of the rod that the water is flowing into.

Next, the script solves a torque balance between the spring that is pushing the buffer against the spiral, and the torque on the rod that is spinning the gear, to solve for the average radius of the gear that spins the disc:

$$2\pi * R_1 * K_1 = 0.5 * p * (U_f^2 - U_i^2) * A - W * K_f \quad (27)$$

After this the “for loop” begins, and the PR value is varied. This solves for the fluid velocity going into the pad that would result in each amount of rotation using another torque balance:

$$P_R * 2\pi * R_1 * K_1 = 0.5 * p * U^2 * A - W * K_f \quad (28)$$

The script then solves a system of equations 28 and 29, where the first equation verifies that the overall change in radius is equal to half the desired change in the bluff body, shown below in Figure 29 and Figure 30. The other equation determines how far into the $x^{0.5}$ function the starting position needs to be in order for the torque from the weak spring to be less than E of the torque on the gear from the flow.

$$\sqrt{x_f} - \sqrt{x_i} = (St * 1.5 * \frac{U_f - U_i}{2 * 180}) \quad (28)$$

$$\begin{aligned} (2 * K_2 * \sqrt{x_i + P_R(x_f - x_i)} - \sqrt{x_i}) * (\sqrt{x_i + P_R(x_f - x_i)} + \frac{\Delta x}{2\pi} * \cos(\tan^{-1}(2 * (x_i + P_R(\sqrt{x_f - x_i})))))) \\ = E * R_1 * (0.5 * p * U^2 * A - W * K_f) \end{aligned} \quad (29)$$

Where K_2 is the weak spring constant.

This returns an initial radius and a starting point for each point of rotation. The square root that relates the increase of the radius of the disc to the water velocity increases the radius by a known amount, but it starts and ends at different points to control the angle that the torque from the weak spring would be exerting on the disc. When it was run for 25 different rotational positions, all of the initial radii were approximately the same at 0.01 m, and the largest starting point which was 358.8 m, with an endpoint of 358.8521 m, with the displacement being 2.08m. From this, the radius of the variable radius disc to be was determined to be:

$$R = 0.01 + \sqrt{\theta} - \sqrt{358.789} \text{ from } \theta = 358.7890 \text{ to } 358.8521 \quad (30)$$

From the values for the area, average gear radius, disc radius, and spring sizes, the mechanism design was able to be modeled. The areas which come into contact with the springs were designed so that they each had a pad that would be slightly bigger than the outside diameter of the spring for it to push against, as well as a small area that is slightly smaller than the inside diameter to help keep the spring in place. The detailed models for each part are shown below, all dimensions are in millimeters.

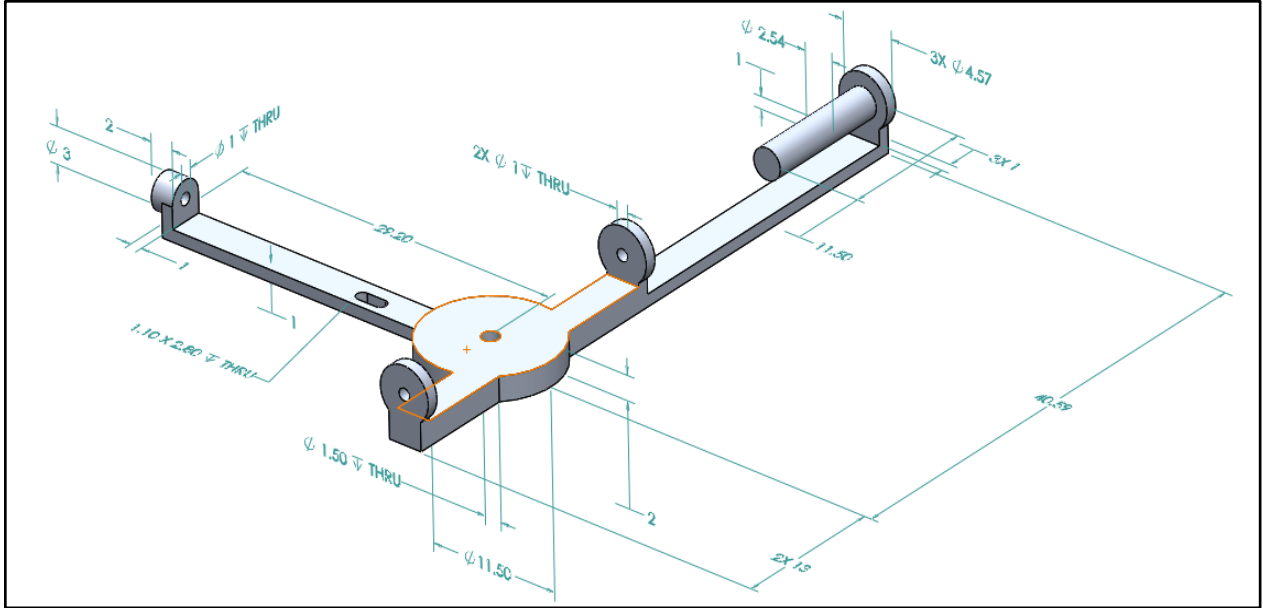


Figure 30: Mechanism Base

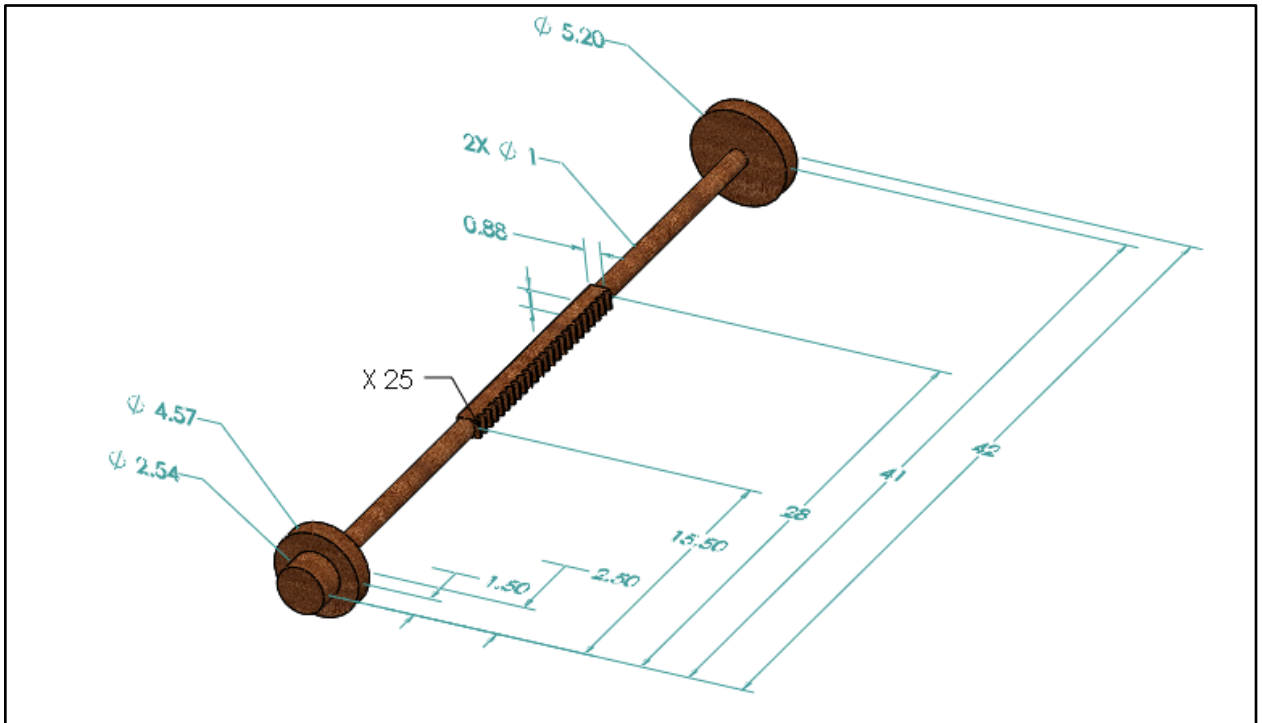


Figure 31: Mechanism Rod

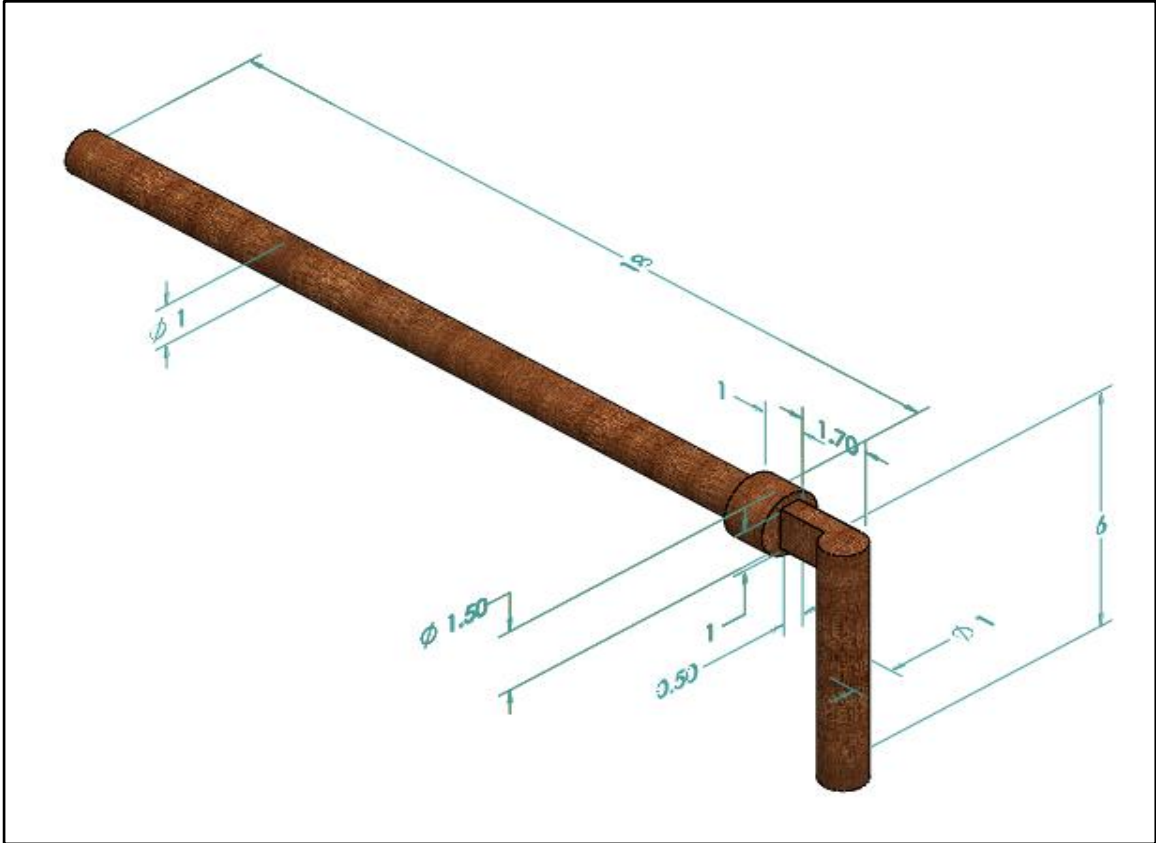


Figure 32: Mechanism Buffer Post

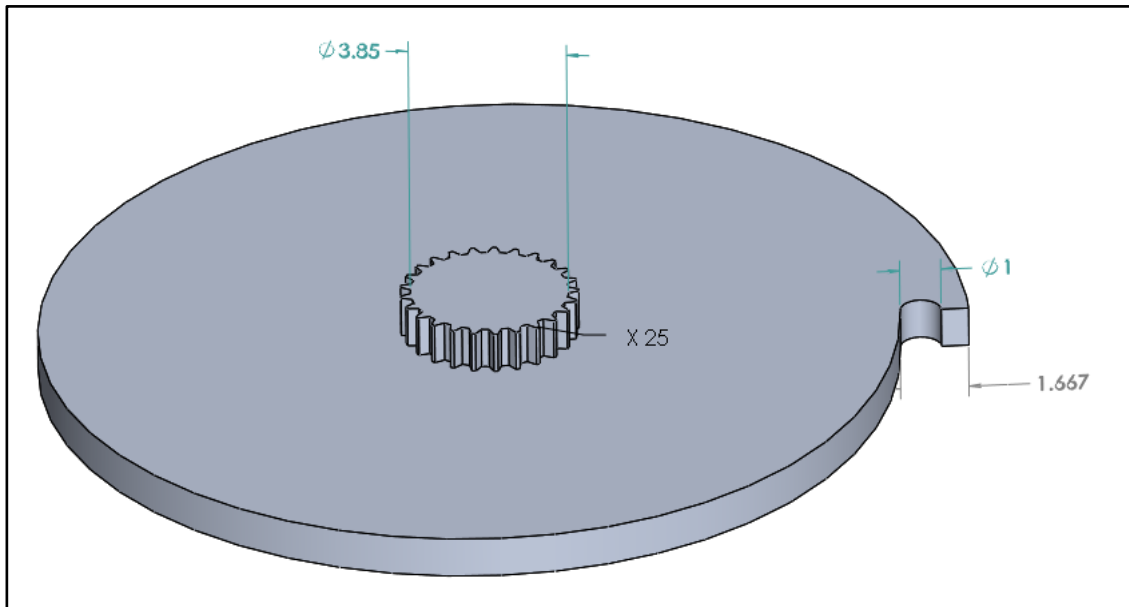


Figure 33: Top View of Mechanism Disk

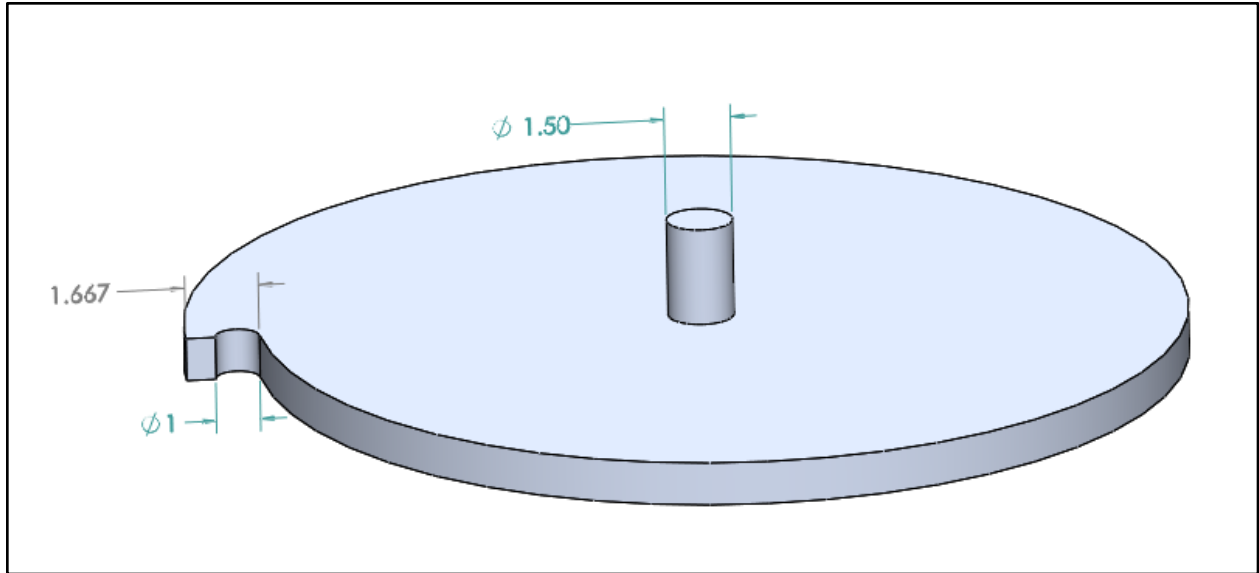


Figure 34: Bottom View of Mechanism Disc

The wood material chosen for the rod would need to be changed for a real-sized model. It weighs too little at 0.05 grams when it is supposed to be approximately 1.4 grams. It was used here arbitrarily since this design is too small and requires too tight of a tolerance to be manufactured at WPI. This means that in order to test it, it will have to be scaled up using the MATLAB script and a different set of larger springs. At the scaled size, wood on metal would give an ideal friction coefficient. If a new material or structure could not be found that weighs the right amount then the springs used in this design will need to be revised, as in the current configuration the rod is too heavy or the friction coefficient between the rod and its support is too high. Additionally, this design will need to be experimentally verified.

4. Nozzle Construction Process

The manufacture of the system was primarily accomplished via additive manufacture. The team went through the WPI Rapid Prototyping system in order to obtain a usable, 3D-printed nozzle prototype. We chose additive manufacturing as our nozzle design emphasized precise tolerances over material strength. Our decision to use additive manufacturing was also influenced by the team’s inexperience with CNC manufacturing as well as the cost and time savings rapid prototyping could provide.

The bluff bodies for the eel design were constructed out of hard plastic sourced from a gift card. This card was cut to approximately 21mm in length. Four distinct width bluff bodies were cut, shown below in Table 5 as required by the variety of bluff sizes needed for testing (discussed further in Section 5.3). These strips of plastic were then adhered to thin metal wires for additional rigidity, as well as enabling them to be slotted vertically such that they would not move horizontally.

Table 5: The Manufactured Bluff Body Sizes.

Bluff Body	Width (mm)
Small Extreme	1.5mm
Large Extreme	5mm
Empirically Determined 1	2.22mm
Empirically Determined 2	3.33mm

The thin-film piezoelectric film in our nozzle was a Measurement Specialties *LDT0* PFVD Solid State Switch/Vibration Sensor. Using thin, solid core wires, the leads of the piezo were soldered such that the piezo was mounted similar to a flag downstream from the bluff body. The fully manufactured nozzle is shown below in Figure 35.



Figure 35: The Fully Manufactured Nozzle

Once the nozzle was completely manufactured, the effectiveness of the nozzle and effectiveness of varying the bluff body needed to be confirmed through testing.

5. Testing and Analysis

The majority of our testing took place in the WPI Crew team rowing tank (Figure 36), located on the WPI Recreation Center's bottom floor. This testing site was chosen as past MQP's have determined the tank has a variable flow rate is capable of producing flows upward of 2.0 m/s, which is within the suitable testing range for the project [17]. There was also ample space for the device to fit in the tank as it is 90" wide, and approximately 10" deep at the away side.

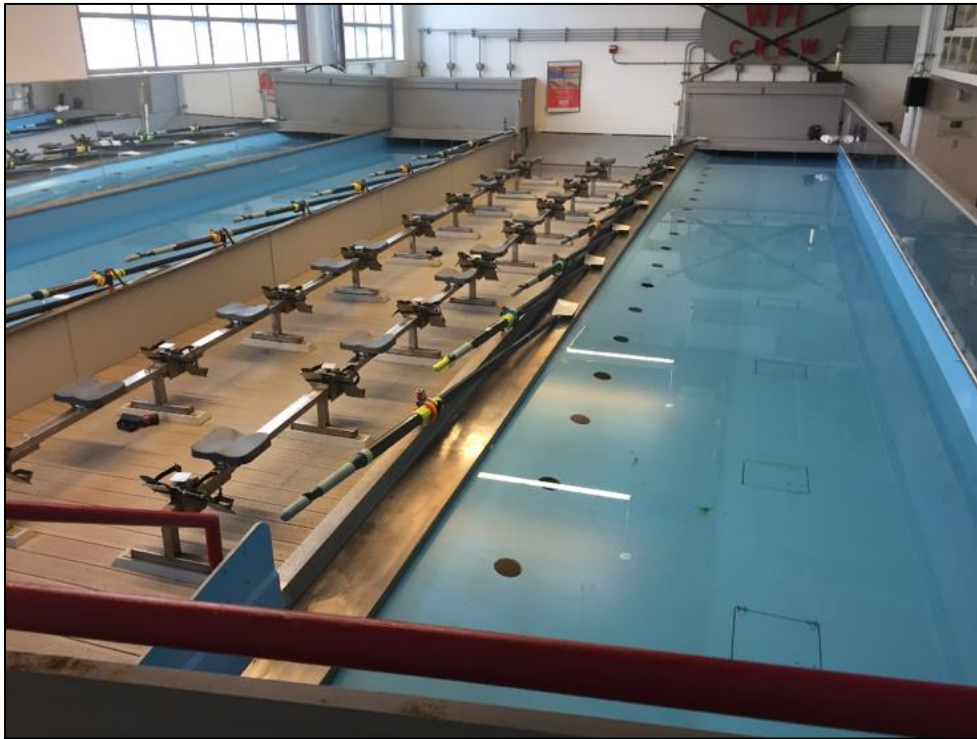


Figure 36: The WPI Crew Team Rowing Tank

5.1 Testing Methodology

Before the device was tested, a means of approximating the local flow velocity within the nozzle needed to be established. It was determined that this could be done via pressure using the equation:

$$V = \sqrt{\frac{2P}{\rho_{\text{water}}}} \quad (31)$$

However, in order to do this, we needed the local dynamic or stagnation pressure P . It was determined we could use two pitot tubes and two pressure sensors to measure the fluid velocity in both the nozzle and in the free stream. Two Honeywell model *NSCDRRN005PDUNV* board-mount differential pressure transducers were chosen, as they are capable of measuring pressure differentials (stagnation pressure minus static pressure). These transducers output an analog voltage that correlates to a differential pressure value between two measured inlet

pressures. One pitot tube was placed in the free-stream to measure the tank water velocity, while another tube was placed within the nozzle to measure the increased water velocity.

5.1.1 Building the Testing Rig

To test the device, we constructed a testing rig out of wooden boards that would be able to suspend the nozzle in the rowing tank. The design can be seen in Figure 37. The main board is a 92" long wooden 2x4. Another wooden 2x4 was screwed to the main board, extending 10" down such that the board remained level in the tank. The face of a third 2x4 was adhered to the side of the main board, extending up (opposite to the previously mentioned 10" 2x4). This last board was included to support a pitot tube for measurement of the velocity distribution in the nozzle compared to a second pitot tube suspended via a wooden arm in the free stream. Two holes were drill-pressed perpendicular to the main board in order to feed through two parallel, $\frac{1}{4}$ " threaded steel rods. The purpose of these rods was to hold the nozzle submerged in the tank, with the upstream face of the nozzle perpendicular to the flow. These rods were fixed to the main board via nuts.

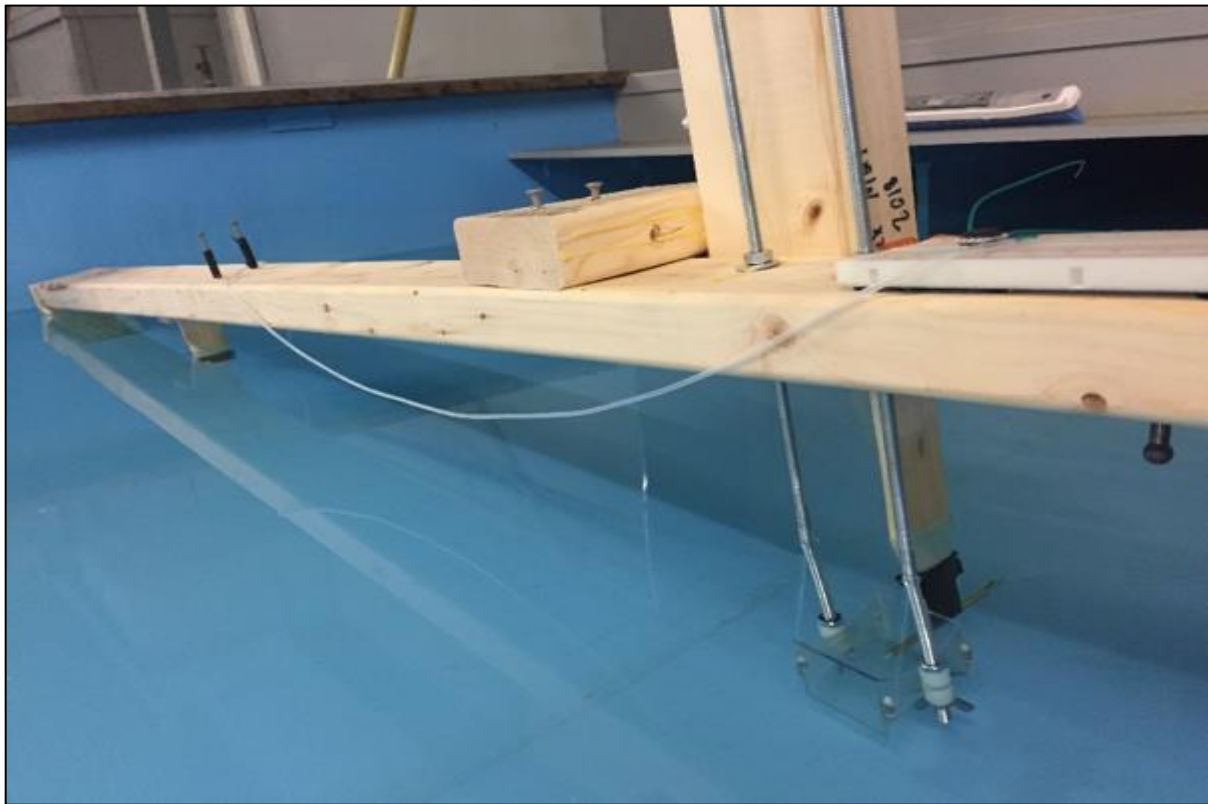


Figure 37: The Testing Rig in the Rowing Tank

5.2 Nozzle Velocity Profile

In order to verify our nozzle design, we determined the flow speed in the nozzle in relation to the flow speed in the free stream. To do so we mounted two pitot tubes onto the

testing rig. One was adhered via a small wooden board to the main rig, and the second one – also attached to a small wooden board – was clamped to the upright 2x4 located roughly midway across the main board. Both pitot tubes were connected via small surgical tubing to their respective pressure transducers. The free stream pitot tube remained at a set depth, while the nozzle’s pitot tube depth varied from the bottom to the top of the inside of the nozzle. Before testing, the pressure transducers were calibrated.

5.2.1 Pressure Transducers and Calibration

The transducers needed to be calibrated to ensure accurate results. This was done by constructing a tall PVC pipe apparatus with a pressure sensor-compatible outlet tube at the bottom, seen in Figure 38. We poured measured volumes of water - correlating to known water depths - into the pipe so that we could calculate the hydrostatic pressures at each volume step. The pressure changes were logged utilizing a National Instruments (NI) digital acquisition box (DAQ) and a custom LabView program that allowed voltage readings to be taken. With the calculated hydrostatic pressures and the corresponding voltage data, both sensors were calibrated.



Figure 38: The Pressure Transducer Calibration Pipe Setup

5.2.2 Pressure Transducer Calibration Results

Our initial calibration of the bluff bodies gave us the following voltage-pressure graphs for the two transducers. One of the two transducers was marked with permanent marker. We refer to this transducer as “marked”, and the other as “unmarked”. The calibration data is shown below in Figures 39 and 40. The resulting line equations represent the relation of transducer output voltage to hydrostatic pressure.

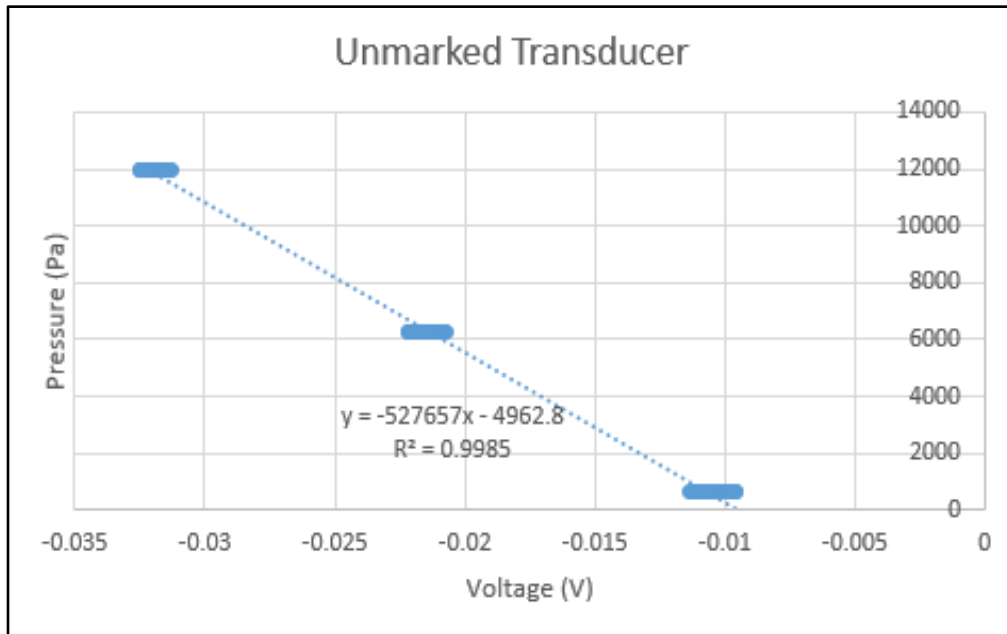


Figure 39: The Initial Unmarked Pressure Transducer Calibration Data

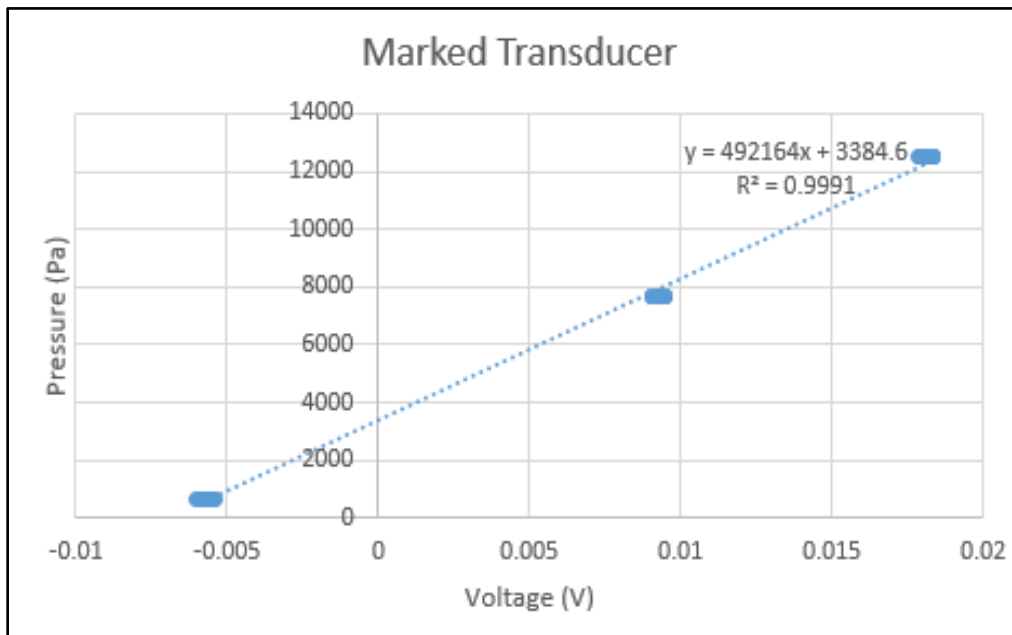


Figure 40: The Initial Marked Pressure Transducer Calibration Data

5.2.3 Velocity Profile Testing Initial Results

For the velocity comparison testing, the flow in the tank was set arbitrarily to 229, which was the value displayed on the tank's flow control system that correlates to the flow through the tank, seen below in Figure 41. A previous MQP had found that 100 units on the control console correlated to roughly 0.1 m/s [17]. Therefore, velocity profile testing took place at approximately 0.23 m/s. The testing rig was placed slightly under halfway along the rowing tank away from the pump end. We then attached two breadboards to the testing rig to mount the pressure transducers to, and then connected their voltage inputs and outputs to the DAQ box.



Figure 41: The Control Panel for the Rowing Tank

For the first test iteration, we aligned the inlet tip of the pitot tube at the bottom of the nozzle as shown in Figure 42. It was important to make sure the tip of the tube remained approximately midway down the length of the nozzle so that the full effects of the nozzle could be recorded. Furthermore, it is important to make sure that the tip of the nozzle aligns precisely parallel with the stream of the flow to capture the exact stagnation pressure. To ensure this we used a spirit level to maintain a constant flat angle for the pitot tube at each height.

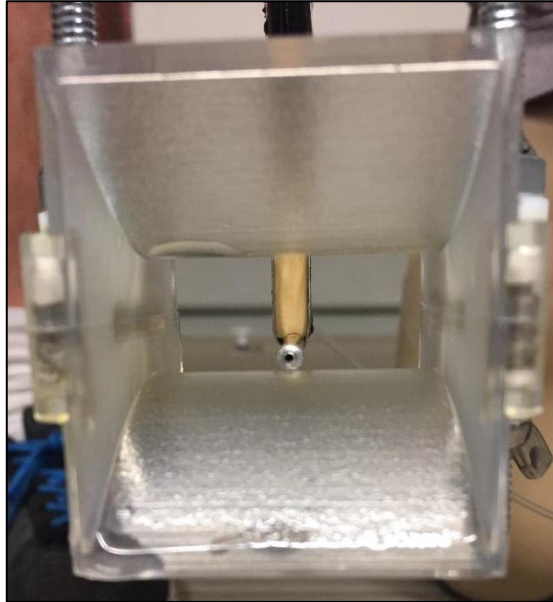


Figure 42: The Pitot Tube within the Nozzle

For the next height iterations, the board containing the pitot tube was raised at approximately 2 mm intervals. Each of these adjustments was checked with a spirit level to assure the pitot tube was completely aligned the same for each test. Data was taken for each 2mm height step until the pitot tube reached the top of the nozzle. The initial results are shown in Figure 43.

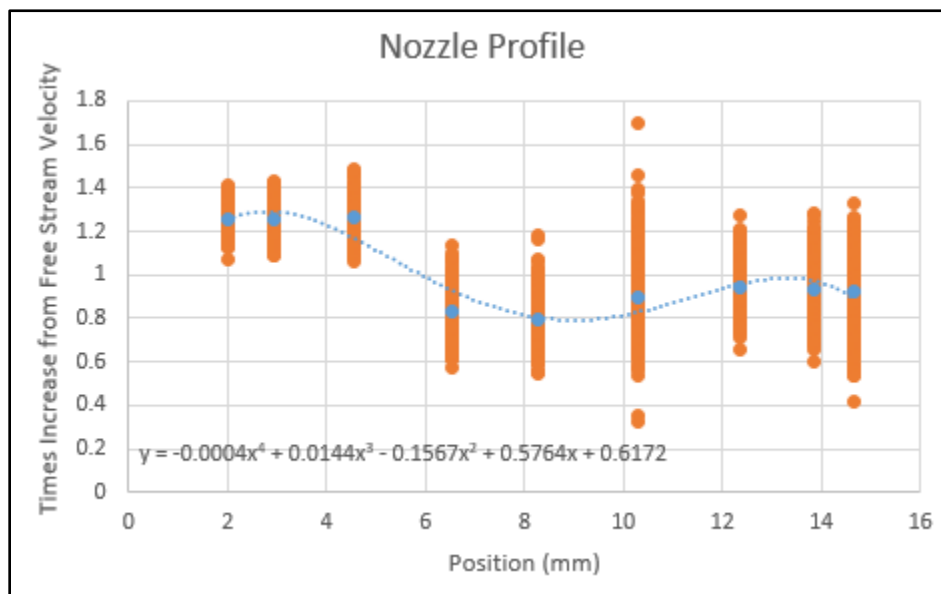


Figure 43: The First Nozzle Velocity Profile

The average free stream velocity appeared to be 1.32 m/s and using the average increase in flow through the nozzle appeared to be 0.98 times, which means there was effectively no

increase in flow speed through the nozzle. These results are suspect, since previous MQP work led us to expect the free stream velocity to be around 0.23 m/s.

5.2.4 Recalibration and Final Velocity Profile Results

Based on the simulations, we were not expecting the nozzle to have a negligible effect on the flow velocity. We decided to re-calibrate the pressure transducers to make sure that we were reading the velocities correctly. Previously, the unmarked transducer was tested with the hydrostatic pressure going into the bottom inlet of the transducer, but this time it was connected to the top. This gave us the results shown below in Figures 44 and 45. The marked transducer showed a large change in the results, while the unmarked transducer numbers were very similar.

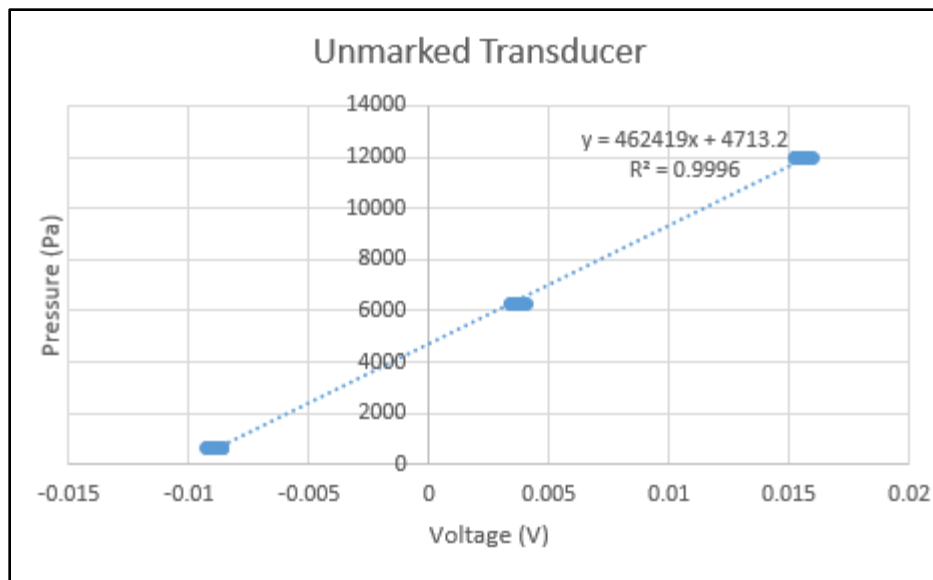


Figure 44: The Updated Unmarked Transducer Calibrations

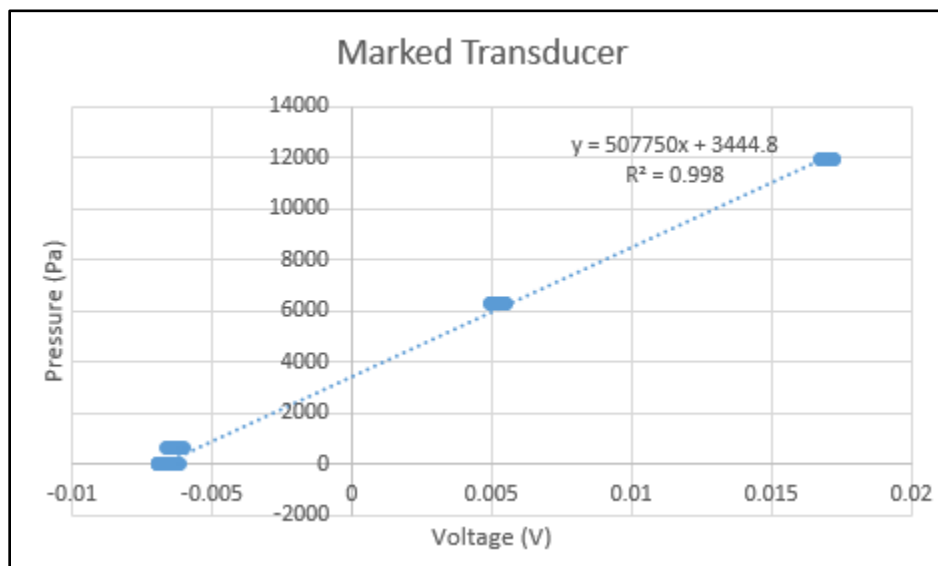


Figure 45: The Updated Marked Transducer Calibrations

Using the same voltage measurements as before, this gave us the increase from free stream profile for the nozzle shown below in Figure 46. This gave us a new average free stream velocity of 0.88 m/s, and an average increase of 1.50 times. While the free stream velocity is closer to the expected 0.23 m/s, it is still much higher.

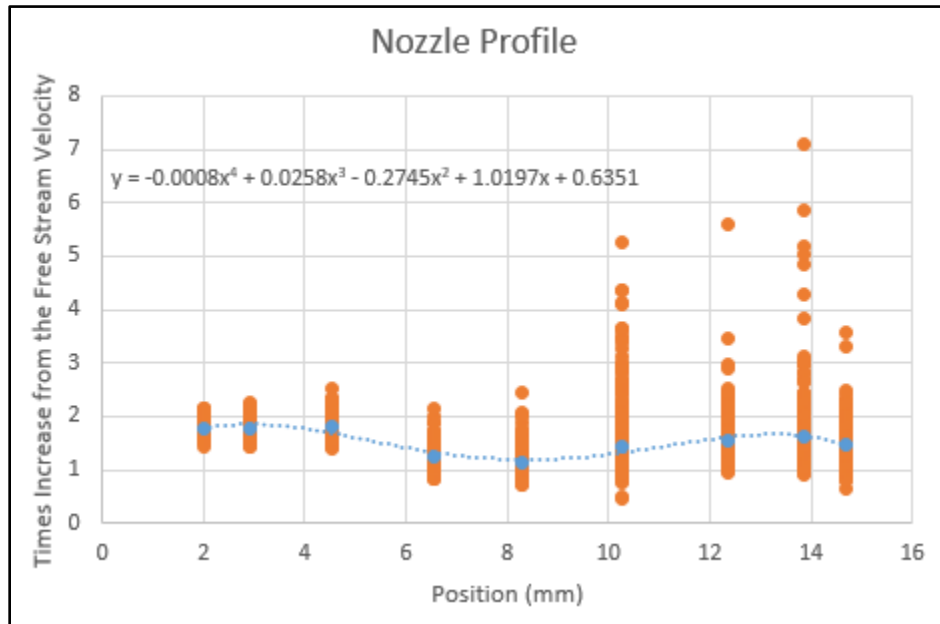


Figure 46: The Nozzle Velocity Profile after Recalibration

5.3 Piezoelectric Testing

Large discrepancies in the velocity profile results led us to pursue two empirically determined bluff body sizes for a flow speed of 2 m/s, shown in above Table 5. The first was chosen for the first result of no increase in flow velocity through the nozzle, and the second was chosen for the 1.50x results. We also tested with two bluff bodies significantly larger and smaller than an optimal theoretical size. Due to the inconsistency of the velocity profile results we decided to utilize a previous group's calibration of the tank's flow speed. Since we primarily aimed to examine the response of the two empirically determined bluff sizes we decided to record data at three flow speeds for these bluffs, while only recording data at 2 m/s flow for the smallest and largest bluffs.

The piezoelectric testing results were divided into two different data sets. These were the average amount of power output by the piezoelectric, and the frequency at which the power was output at. Data was taken using a custom LabView program and the previously used portable DAQ. The data was taken at 1000 samples per second for 10 seconds. This rate was chosen since we expected the highest frequency to be 400 Hz for the smallest bluff body, so in order to reach the Nyquist frequency it would need to be taken at over double that value.

5.3.1 Piezoelectric Testing Power Output Results

To determine a power output, we used a 1kΩ resistor that was specifically measured to be 991Ω on a multimeter. A 1kΩ resistor was chosen such that a +/-1V output would produce a

current of 1mA, which would keep measurement analysis simple. This was placed in series with the output leads the DAQ. To get an idea of the mean power output, we took the average amplitude of the voltage output waveform for the 10 seconds of data. The average voltage V was chosen to get a sense of the typical peak-to-peak value of the output. Equation 32 was then used to determine the average power output. This data is shown in Table 6.

$$P = \frac{V^2}{R} \quad (32)$$

Table 6: Piezoelectric Power Output Data

Bluff Body Size (mm)	Flow Velocity (m/s)	Average Power Output (μ W)
1.50 mm	2.00	0.104
2.22 mm	0.50	0.0347
	1.25	0.0344
	2.00	0.0332
3.33 mm	0.50	0.0347
	1.25	0.0344
	2.00	0.0354
5.00 mm	2.00	0.0757

5.3.2 Piezoelectric Testing Frequency Results

To obtain the frequency results, a Fast Fourier Transform (FFT) function was performed on the output voltage data as it was recorded in LabView. Plots of the data showed a visible peak near the dominant frequency, as shown in Figure 47 below. The dominant frequency of the data set was then approximated to be the frequency of the vortex street. The output data is shown below in Table 7. The complete set of the frequency output graphs is available in Appendix B.

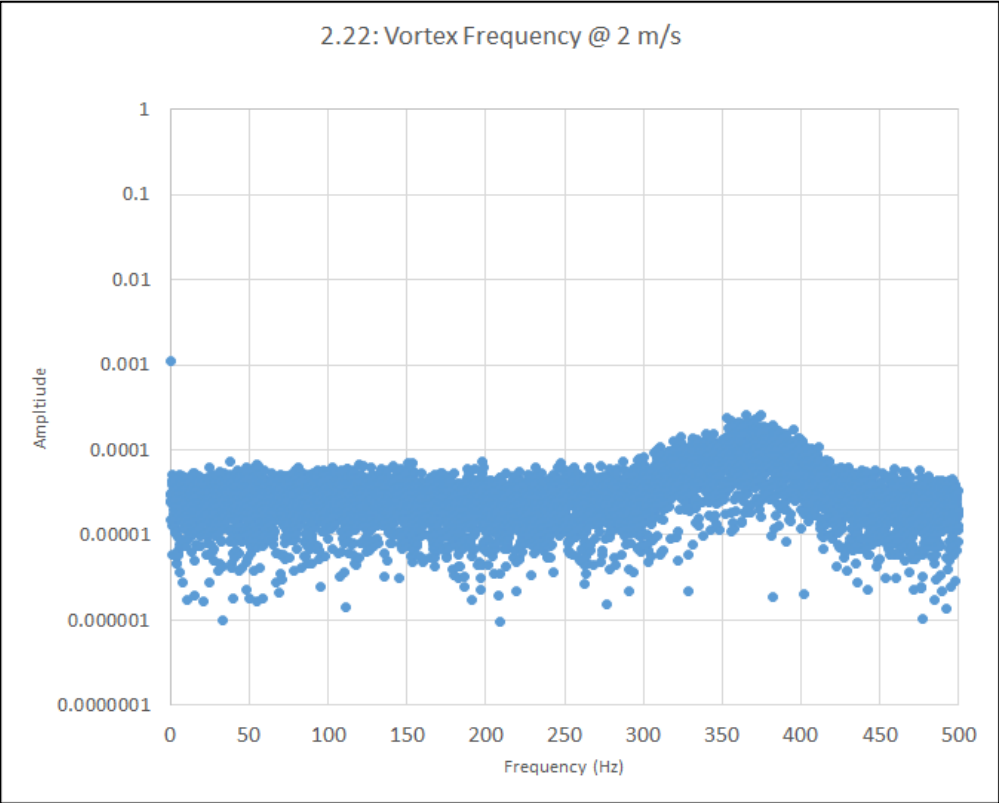


Figure 47: An example output chart of the frequency data.

Table 7: Piezoelectric Frequency Data

Bluff Body Size (mm)	Flow Velocity (m/s)	Approximate Output Frequency (Hz)
1.50 mm	2.00	440
2.22 mm	0.50	380
	1.25	370
	2.00	360
3.33 mm	0.50	495
	1.25	450
	2.00	475
5.00 mm	2.00	275

5.4 Results Discussion

5.4.1 Power Output

Given the piezoelectric we used, we were not expecting a large power output, therefore we found it acceptable to obtain an output at the nanowatt scale. We specifically did not expect a large power output because the *LDT0* thin film piezoelectric we used was supposed to be used as a simple vibration sensor, not a power generator. The piezoelectric we chose produces a maximum output charge on the nanoCoulomb scale, which puts the overall expected current and power output at a very low scale. However, this piezo element's use in this project was to provide a measurable output as a proof-of-concept. The output voltages were on the millivolt scale, the power was on the nanowatt scale, and the waveforms for each of the power outputs were fairly consistent. The output waveforms were not flawless AC waveforms, likely due to the range of frequencies causing the piezoelectric to bend inconsistently.

5.4.2 Frequency

The dominant frequencies found from the FFT are not what was expected. The target frequencies for each bluff body are shown in Table 8. As shown in the table, we expected to see lower frequencies compared to what was actually observed.

Table 8: The Target vs. Actual Frequencies

Bluff Body Size (mm)	Free Stream Velocity (m/s)	Expected Freq. for 1x Free Stream Velocity (Hz)	Expected Freq. for 1.5x Free Stream Velocity (Hz)	Actual Frequency (Hz)
1.50 mm	2.00	267	400	440
2.22 mm	0.50	45	68	380
	1.25	113	170	370
	2.00	180	270	360
3.33 mm	0.50	30	45	495
	1.25	75	113	450
	2.00	120	180	475
5.00 mm	2.00	80	120	275

The large discrepancies with our results suggests that there were either errors in the theory or in the testing set up. Since the frequency changed considerably with each bluff body size, we suspected that the issue was with the theory. To see if the Strouhal number was misestimated, we calculated what it would be from the measured frequencies, using the nozzle

increase of 1.5 times, as there must have been a velocity increase in the nozzle in order to get frequencies this high. This gave us a range of Strouhal numbers between 0.22 and 2.22, which starts out reasonably but becomes excessively large. The inconsistencies in these Strouhal numbers suggests that the issue is not in the estimation of the Strouhal number. We then used our estimated Strouhal number of 0.2 to calculate what the nozzle increase would need to be in order to hit these frequencies. This gives an increase range of 1.65 times to 16.65 times, which like the Strouhal number calculations, starts out reasonably but then becomes inordinately large.

Table 9: The Strouhal Numbers and Estimated Velocity Increases of the Nozzle

Bluff Body (mm)	U (m/s)	Measured frequency (Hz)	St (with a nozzle increase of 1.5x)	Times increase from the nozzle (with $St = 0.2$)
1.50 mm	1.50	440	0.22	1.65
2.22 mm	0.50	380	1.12	8.44
	1.25	370	0.44	3.29
	2.00	360	0.27	2.00
3.33 mm	0.50	500	2.22	16.65
	1.25	450	0.80	5.44
	2.00	475	0.53	3.95
5.00 mm	2.00	275	0.46	3.44

These wide ranges suggest that neither the approximation for the Strouhal number nor the increase in flow from velocity was solely produced the off results, but it could be a combination of both.

6. Conclusions

The disparity between the higher power generation seen in the largest and smallest bluff bodies and our expectation of them as the worse power generators, suggest that there were sources of external error in addition to the discrepancies mentioned in section 5.4.2. The large range of flow increases and Strouhal numbers from the analysis shown in Table 9 suggest that neither our approximation for the Strouhal number nor the nozzle flow increase are solely responsible for our unexpected results. However, our proof-of-concept device did produce a measured power output.

6.1 Testing

We could have encountered testing errors in many places during our experiment. The rowing tank's pump was noticeably vibrating the tank, which would at least contribute to the noise we measured, but likely not the 400 Hz dominant frequencies we observed. The flow in the tank may be Womersley Flow, as the flow appeared to vary periodically due to the tank's pump. However, the pulsation frequency would not change with the size of the bluff body. If it drove the unexpected dominant frequency, it would have been approximately constant for all of the runs at a specific pump setting. For example, the frequency of 275 Hz for the 5 mm bluff body drastically differed from the 430 Hz that the 1.5 mm bluff body produced.

Previous MQP's have found that the flow velocity fluctuates significantly in the rowing tank. Flow velocity fluctuations could lead to data inconsistent with the expected results for changes in bluff body size. Ambiguities in the flow velocity represent the most likely source of error from the testing setup, and almost definitely contributed to the unexpected frequencies and power outputs. Due to potential errors in theory, we cannot conclude the exact extent to which the testing setup affected the results.

6.2 Theory

The design considerations we made for the bluff bodies and the positioning of the piezoelectric material are also a potential source of error. The largest Reynolds number which occurred for the largest bluff body was approximated as 15,000. This is within the range in which the Strouhal number is approximated as 0.2, but this is setup-dependent and it is possible that the nozzle assembly has a larger Strouhal number. This possibility could help explain the unexpectedly high frequencies.

The possibility of a delay between the vortex shedding frequency and the frequencies of the vortices acting on the piezoelectric film was not accounted for. This delay would be due to the time it takes for the flow to carry the vortices along the distance between the bluff body and the film, which is represented by Equation 33.

$$T = l/U_{inf} \quad (33)$$

Where T is the period of time it takes for vortices to reach the piezoelectric film, l represents the distance the shed vortex travels, and U_{inf} is the free stream velocity around the bluff body.

Additionally, the piezoelectric film could be vibrating at a resonant frequency other than the one listed by the manufacturer. It was expected to vibrate at the first resonant frequency of 180 Hz. It is possible that the resonant frequency for the second mode of vibration was near 400 Hz, approximately what we measured most of our dominant frequencies at.

6.3 Further Considerations

A key improvement that could be made on this project would be to perform a similar test under more stable testing conditions. The WPI rowing tank has been shown to deliver inconsistent flow velocities, with increased fluctuation amplitudes at higher flow settings. A more stable testing location could provide a more consistent vortex street. Along with a better testing environment, a less error-prone apparatus to calibrate the pressure transducers would allow more accurate determination of the nozzle effectiveness.

An improved testing environment would reduce testing errors; however, there would still be design issues to address. The Strouhal number for the specific nozzle set up, the frequency of the vortices acting on the film, the different resonant frequencies of the piezoelectric film, and the effectiveness of the nozzle would need to be determined either empirically or numerically. Additionally, the more complex nozzle simulations ran into memory issues when performed the design studio computers. They ended up using up all 64 gigabytes of available RAM, which meant that they had to be run at lower, potentially less-accurate mesh settings.

Another consideration would be to explore the electrical aspects of the project. Three potential avenues exist for optimizing the power output of the system. The first way would be to utilize a more power generation-suitable piezoelectric transducer compared to the simple sensor used in this project. Many are commercially available with a wide range of resonant frequencies, so there is a potential for a more efficient deployment of the system with a better suited piezoelectric element. A second way the power output could be explored could be to utilize an array of multiple piezoelectric elements in parallel for an increased current output, or in series for an increased voltage output. A third option would be to vary the resistor size to find what would be optimal for the highest power output, as this project only tested a single resistance value.

6.4 Potential Applications

Our project set out to provide a viable solution for powering remote low-power applications, including river-based water quality sensors. Despite discrepancies in our results, we have produced a design capable of consistently producing over 30nW in flow speeds from 0.5 to 2 m/s. Although this figure is small, experimental sensors exist at that power level, and there is potential to improve design performance through future work [5]. Our project has successfully produced a device potentially capable of powering very low-power applications.

As we tested our device in flow speeds up to 2 m/s, we can say that our design is durable enough to withstand large flow speeds, at least temporarily. Long-term durability and performance under expected environmental conditions (i.e. impacts of debris, aquatic life, and temperature fluctuations) must be answered through future prototyping and experimentation.

References:

- [1] Chih-Ying Chen, <https://plus.google.com/+ChihYingChen/posts/ThdnyWcwC7x>. 2017.
- [2] United States Geological Survey, 'What is continuous real-time water quality (RTWQ)?', 2014. [Online]. Available: http://waterwatch.usgs.gov/wqwatch/faq?faq_id=1. [Accessed: 5-Sept-2017].
- [3] Dibin Zhu (2011). Vibration Energy Harvesting: Machinery Vibration, Human Movement and Flow Induced Vibration, Sustainable Energy Harvesting Technologies - Past, Present and Future, Dr. Yen Kheng Tan (Ed.), ISBN: 978-953-307-438-2, InTech, Available from: <http://www.intechopen.com/books/sustainable-energyharvesting-technologies-past->
- [4] In-Situ Inc., "Water Quality Testing Equipment Products," In-Situ Inc., 2017. Available: https://in-situ.com/wp-content/uploads/2015/09/SS_AquaTROLL_600_June2017PQ.pdf
- [5] (August 8,). Millimeter Scale Energy Harvesting Based Sensors. Available: <https://www.digikey.com/en/articles/techzone/2012/aug/millimeter-scale-energy-harvesting-based-sensors>.
- [6] Williamson, S. J., B. H. Stark, and J. D. Booker. "Low head pico hydro turbine selection using a multi-criteria analysis." *Renewable Energy* 61 (2014): 43-50. Available: http://www.ep.liu.se/ecp/057/vol6/001/ecp57vol6_001.pdf. [Accessed: 02- Oct- 2017].
- [7] S. Anderson, 'The Use of the Helical Turbine in River Currents', 2009. [Online]. Available: http://globalcoral.org/wp-content/uploads/2014/01/Helical_Turbine_for_River_Currents_Sept2009_corrected.pdf. [Accessed: 12- Sept- 2017].
- [8] A. Techet, "13.42 Lecture: Vortex Induced Vibration", M.I.T., 2005.
- [9] "Von Karman Vortex Street at $Re = 250$ ", Dolfyn.net, 2017. [Online]. Available: <https://www.youtube.com/watch?v=IDeGDFZSYo8>. [Accessed: 12- Oct- 2017].
- [10] A. Roshko, "On the development of turbulent wakes from vortex streets", Ph.D, California Institute of Technology, 1952.
- [11] R. Maddy, "VORTEX SHEDDING FROM SQUARE PLATES NEAR A GROUND PLANE: AN EXPERIMENTAL STUDY", Master of Science in Mechanical Engineering, Texas Tech University, 1979.
- [12] M. Kim and J. Kim, "Effect of Reynolds Number and Aspect Ratio of Geometry on the Unsteady Flow Physics around a Rectangular Parallelepiped", in *Applied Aerodynamics Conference*, Chicago, 2010, pp. 1-11.
- [13] J. Marshall, "A criterion for vortex street breakdown", *Physics of Fluids A: Fluid Dynamics*, vol. 3, no. 4, pp. 588-594, 1991.

- [14] Allen, J. J., and A. J. Smits. "Energy harvesting eel." *Journal of fluids and structures* 15, no. 3-4 (2001): 629-640.
- [15] Koyvanich, K., Smithmaitrie, P. and Muensit, N., 2015. Perspective microscale piezoelectric harvester for converting flow energy in water way. *tc*, 2, p.2.
- [16] M. Bernitsas, "The VIVACE Converter: Enhancing Flow Induced Motions to Harness Hydrokinetic Energy in an Environmentally Compatible Way," Boulder, CO, 2011]]
- [17] Natalie Diltz et al, "Vortex induced vibration energy harvesting through piezoelectric transducers," Worcester Polytechnic Institute, Worcester, MA, 2017.
- [18] D. Distler, B. Johnson, M. Kielbasa, B. Phinney, "Optimization of Oscillating Body for Vortex Induced Vibrations," Worcester Polytechnic Institute, Worcester, MA, 2011]
- [19] C. Woodford, "Piezoelectricity - How does it work? | What is it used for?", *Explain that Stuff*, 2017. [Online]. Available: <http://www.explainthatstuff.com/piezoelectricity.html>. [Accessed: 17- Sep- 2017].
- [20]"Principles and Applications of Piezoceramics", *Beijing Ultrasonic*, 2017. [Online]. Available: <https://www.bjultrasonic.com/ultrasonic-technical-info/piezoelectric-ceramic-technical/>. [Accessed: 17- Sep- 2017].
- [21] "Piezoelectric Energy Harvesting Kit", *Piezo.com*, 2017. [Online]. Available: <http://www.piezo.com/prodproto4EHkit.html>. [Accessed: 05- Oct- 2017].
- [22] A. Arnau, *Piezoelectric transducers and applications*, 2nd ed. New York: Springer, 2010, pp. 2-46.
- [23] "Piezo Protection Advantage", Mide Technology, 2017. [Online]. Available: <https://www.mide.com/collections/piezo-protection-advantage-ppa>. [Accessed: 12- Oct- 2017]
- [24] R. Tiwari, K. Ryoo, A. Schlichting and E. Garcia, "Extremely low-loss rectification methodology for low-power vibration energy harvesters", *Smart Materials and Structures*, vol. 22, no. 6, p. 062001, 2013.
- [25] C. Choi and D. Kwon, "Wind tunnel blockage effects on aerodynamic behavior of bluff body", *Wind and Structures*, vol. 1, no. 4, pp. 351-364, 1998.

APPENDIX A: MATLAB Script for Mechanism Design.

```
clear all;
N=25;
Def=0.0125;
K1=5.197;
Uf=2.5;
Ui=0.5;
p=1000;
Kf=0.2; % Wood on wet metal etc
Kf2=0.2;
St=0.2;
f=180;
K2=0.0734;
n=1.5;
E=0.05 ; % Error
Xi2=ones(1,N);
Xf2=ones(1,N);
R22=ones(1,N);

syms A W
Dummy1=Def*K1==0.5*p*Uf^2*A-W*Kf;
Dummy2=0==0.5*p*Ui^2*A-W*Kf;
Dummy3=vpasolve([Dummy1 Dummy2],[A W],[0 inf]);

A=Dummy3.A;
W=Dummy3.W;

syms R1
R1=vpasolve(2*pi*R1*K1==0.5*p*(Uf^2)*A-W*Kf,R1);

for i=1:N
PR=1/N*i; % % Rotation

syms U
U=vpasolve(PR*2*pi*R1*K1==0.5*p*U^2*A-W*Kf,U,[0 inf]);

syms X Xi Xf
% displacement
Dummy5=Xf^0.5-Xi^0.5==St*n*(Uf-Ui)/(2*180);
% torque
Dummy6=2*K2*((Xi+PR*(Xf-Xi))^0.5-Xi^0.5)*((Xi+PR*(Xf-Xi))^0.5+(Xf-Xi)/(2*pi))*cos(atan(2*(Xf-Xi)/(Xi+PR*(Xf-Xi)^0.5)))==E*R1*(0.5*p*U^2*A-W*Kf);
Dummy7=vpasolve([Dummy5 Dummy6],[Xi Xf]);

Xi2(i)=Dummy7.Xi;
Xf2(i)=Dummy7.Xf;

R22(i)=(Xf2(i)-Xi2(i))/(2*pi);

end
```

APPENDIX B: Fast Fourier Transform Chart for Piezoelectric Output Data.

The following FFT graphs display the dominant frequencies for each bluff body size (1.5, 2.22, 3.33, and 5 mm) at listed velocities.

